NTNU – Trondheim
Norwegian University of
Science and Technology

Atomistic Implications of Stacking Fault Energy on Dislocation - Void Interactions

Øyvind Storesund Hetland

Master of Science in Physics and Mathematics
Submission date: October 2012
Supervisor: Ingve Simonsen, IFY
Co-supervisor: Jon Samseth, NTNU
Taira Okita, University of Tokyo

Norwegian University of Science and Technology
Department of Physics

Abstract

Irradiation hardening due to voids can be a significant effect of radiation damage in metals, but treatment of this by elasticity theory of dislocations is difficult when the mechanisms controlling the obstacle strength are atomic in nature. Copper has long been used to approximate austenitic stainless steels in computer simulations because of their shared face-centered cubic structure and similar Stacking Fault Energy (SFE). Their stacking fault properties are however not identical; the SFE in stainless steel is significantly lower than that in Cu. Low values of SFE lead to wide dissociation of dislocations in their glide planes into Shockley partial dislocations, severely affecting the hardening process of the metal.

Molecular Dynamics simulations have been conducted in order to highlight the implications of stacking fault energy on the interaction between dissociated dislocations and nanoscale voids. A recently developed set of interatomic potentials with a range of stacking fault energies based on FCC copper was used in order to investigate the Critical Resolved Shear Stress (CRSS) and other interaction details for a range of void sizes, temperatures, impact parameters and void separation distances for both edge and screw dislocations.

Changes in SFE were found to affect the pinning interactions for dissociated edge dislocations in a relatively weak but systematic manner. The CRSS needed for any given dislocation to overcome the array of voids was in all cases shown to decrease with decreasing SFE and *vice versa.* This was also concluded for dissociated screw dislocations, but with an extra layer of complexity: The advent of complex cross-slip mechanisms sometimes lead to highly unpredictable void pinning dynamics, mainly through multiple cross-slip and its consequences; the creation of temporary immobile dislocation structures. The value of SFE is shown to be very influential on the distribution, probability and form of complex cross-slip mechanisms, which may double or triple the pinning strength of voids.

Sammendrag

Herding på grunn av nano-hulrom ("voids") er en viktig sideeffekt av stålingsskader i metaller, men det har vist seg krevende å beskrive disse forholdene ved bruk av elastisitetsteori for dislokasjoner når mekanismene som kontrollerer styrken til de introduserte hindringene er atomistiske. Kobber (Cu) har lenge blitt brukt til å etterligne austenittisk rustfritt stål i datasimuleringer på grunn av deres delte kubisk flatesentrerte materialstruktur og lignende verdier for stablefeilsenergi (flatefeil, "Stacking Fault Energy", SFE). Deres SFE-egenskaper er imidlertid ikke identiske: SFE for austenittisk rustfritt stål er markant lavere enn for kobber. Lave verdier av SFE fører til en ekstra vid dissosiasjon av dislokasjonene i deres glideplan. Dermed øker også likevektsavstanden mellom de resulterende Shockley partielle dislokasjonene. Dette har en betydelig innvirkning på herdingsprosessene i metallet.

Molekylærdynamiske simuleringer ("Molecular Dynamics", MD) har blitt utført med hensikt i å fremheve implikasjonene av SFE-verdi på interaksjoner mellom dissosierte dislokasjoner og nano-hulrom. Et nyutviklet sett med kobber-baserte inter-atomiske potensialer som spenner over et utvalg av SFE-verdier ble i denne oppgaven brukt til å undersøke kritisk skjærspenning ("Critical Resolved Shear Stress", CRSS) og andre interaksjonsdetaljer for et utvalg hulroms-størrelser, temperaturer, kryssparametere og hulromsseparasjoner for både kantdislokasjoner og skruedislokasjoner.

Hindringsstyrken til kantdislokasjoner ble påvirket av SFE på en relativt svak men systematisk måte. Den kritiske skjærspenningen som til enhver tid krevdes av dislokasjonene for muliggjøre en passering av hulrommene ble redusert ved reduserte SFE-verdier og vice versa. Den samme konklusjonen ble nådd for skruedislokasjoner, men med et ekstra lag av kompleksitet: Kompleks rotasjonsglidning førte tidvis til en meget uforutsigbar hulromsinteraksjon, som oftest gjennom flerfoldig rotasjonsglidning og dets konsekvenser ved dannelser av midlertidige immobile dislokasjonsstrukturer. Materialverdien av SFE blir i rapporten vist å ha en markant innvirkning på både distribusjonen av, formen til og sannsynligheten for rotasjonsglidning, som kan både doble og tredoble hindringsstyrken til nano-hulrommene.

Preface

This report is the result of thesis work carried out at the University of Tokyo, School of Engineering, for the Department of Physics at the Norwegian University of Science and Technology (NTNU) during the summer semester of 2012. The extent of the thesis is 30 ECTS, suggesting an estimated workload of 40 hours per week. This master's thesis is the conclusion of a five-year integrated "Master in Science"-programme in applied physics and mathematics provided by NTNU.

The effort put into this project has provided me with a valuable glimpse into a world that has become increasingly important for the applied physicist and engineer: the world scientific computing and modeling. The project has been both rewarding and educational, and I am very happy with the results obtained in a relatively small amount of time.

I feel privileged for having had the opportunity to work with Professor Taira Okita and his team at the University of Tokyo. I am indebted to my cooperation partner Keisuke Asari in the Okita laboratory group for his valuable insight and discussions, and for his inclusiveness in letting me work on topics related closely to his research. Kato Satoshi, thank you for your never failing encouragement and feedback. I would like to thank Professor Ingve Simonsen at NTNU for his support, guidance, patience and open door philosophy. Professor Jon Samseth has also been of valuable help and support. Finally, I am truly grateful to Laura Kay Brodbeck, whose unfailing support and encouragement makes all the difference in the world.

Øyvind Storesund Hetland,
Trondheim, September 2012

Contents

Chapter 1

Introduction

Designing materials that can withstand radiation-induced damage is important for improving the reliability, safety and lifespan of all nuclear systems. When designing nuclear reactors or the materials that go into them, one of the key challenges is finding materials that can withstand an outrageously extreme environment. In addition to the constant bombardment by radiation, reactor materials may be subjected to extremes in temperature, physical stress, and corrosive conditions. Austenitic stainless steel has proven to be a resistant material in all these respects, and is therefore used extensively in both common and exotic power plant designs. However, material defects formed by radiation damage are responsible for significant changes in mechanical properties over time such as yield stress, work hardening rate and ductility [1, 2, 3]. (An example of hardening is displayed in Figure 1.2.) Thus, the ability to both accurately and precisely predict material degradation, such as irradiation hardening in austenitic stainless steels, is of both great value and significance.

Voids, as formed by supersaturations of vacancies, are ubiquitous in irradiated metals and act as obstacles to dislocation motion. This results in an increase of critical stress, and voids therefore contribute to material hardening. Treatment of these obstacles by elasticity theory of dislocations is difficult when the mechanisms controlling the obstacle strength are atomic in nature, operating well below the length scale open to direct experimental study. Predictive models based on the continuum framework of elasticity theory therefore require information from atomic-level simulation in order to perform to a satisfactory degree.

Modern computing power combined with reliable interatomic potentials have turned Molecular Dynamics simulation (MD) into a very general method of simulation. MD is a simulation technique where the time evolution of a set of interaction atoms is followed by integrating their classical equations of

motion. Such simulations may provide information about the partitioning of energy between elastic interactions and purely atomistic effects, and possibly reveal new phenomena which cannot be dealt with in the elastic description [4].

A *stacking fault* in a crystal is a planar defect, a local region where the regular stacking sequence has been interrupted. This increases the energy of the crystal, measured by the stacking fault energy (SFE). Copper (Cu) has long been used to approximate austenitic stainless steels (ASS) in computer simulations, amongst others because of their shared face-centered cubic (FCC) structure and similarity in SFE. Their stacking fault properties are however not identical; the SFE of ASS is significantly lower than that of Cu. Low values of SFE lead to wide dissociation of dislocations in their glide planes into Shockley partial dislocations, severely affecting the hardening process of the metal. A set of interatomic potentials for MD simulations based on copper with a range of different stacking fault energies has recently been developed by Mikhail Mendelev (U.S. Ames Laboratory). These potentials enable us to investigate the influence of SFE on dislocation-void interaction mechanisms through atomistic MD simulations.

The aim of the research presented in this report is to highlight the implications and effects of SFE on the atomistic interactions between dissociated dislocations and nanoscale voids, with the purpose of both expanding our understanding of these processes and improving on the material predictability.

The defect we consider as the obstacle to dislocation glide is the recently mentioned void, and there are several reasons for this choice. It is perhaps the simplest obstacle formed by a cluster of point defects, i.e. it has no dislocation character so the complication of dislocation–dislocation reactions is avoided. Voids are commonly observed in irradiated metals: studies have suggested that irradiation hardening is dominated by voids and dislocation loops at 300-400°C [3]. This is a typical operating temperature of in-service nuclear reactors. Extensive research on dislocation-void interaction has recently been conducted by Osetsky *et al.* in [5] and Hatano *et al.* in [6, 7]. Some, but not all of the data found for the strength of voids is consistent with results in the literature obtained using elasticity theory. Their investigations have revealed several interesting interaction effects that are consequences of the dislocation dissociation found in Cu, suggesting that a better understanding of the influence of the dissociation width on the interaction mechanisms, and thereby the value of SFE, is needed.

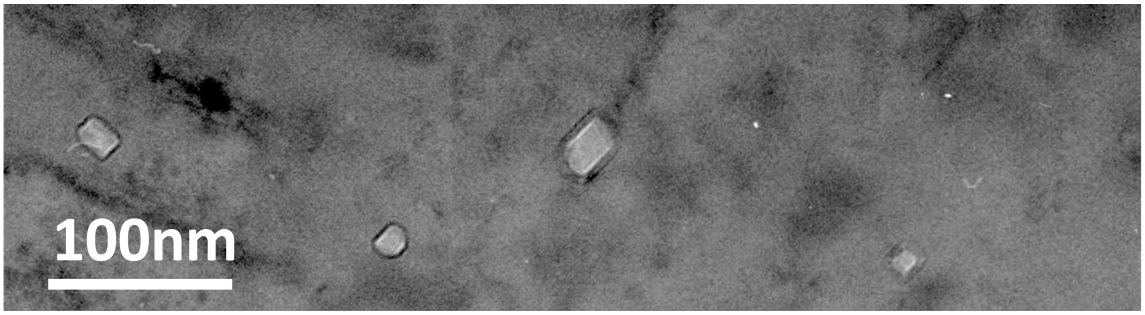

Figure 1.1: Transmission Electron Microscope (TEM) image showing voids created in a low-dpa ($\approx$ 0.1dpa) environment. Irradiation temperature: 415^{o}C.

In this thesis, the pinning dynamics of dissociated edge and screw dislocations with voids in copper are investigated by means of Molecular Dynamics (MD) simulations. Focus is kept on the influence of stacking fault energy on these interactions.

The contents of this report is organized as follows: In Chapter 2, some background material is presented and discussed, as well as selected theory crucial for the interpretation of the simulation methods and results. Chapter 3 presents the conditions and models used for MD simulations in this thesis. The simulation results are presented together with relevant interpretation and discussion in Chapter 4. We then conclude our findings in Chapter 5. The Appendix contains tabulated information on the interatomic potentials provided by Mendelev and Mishin.

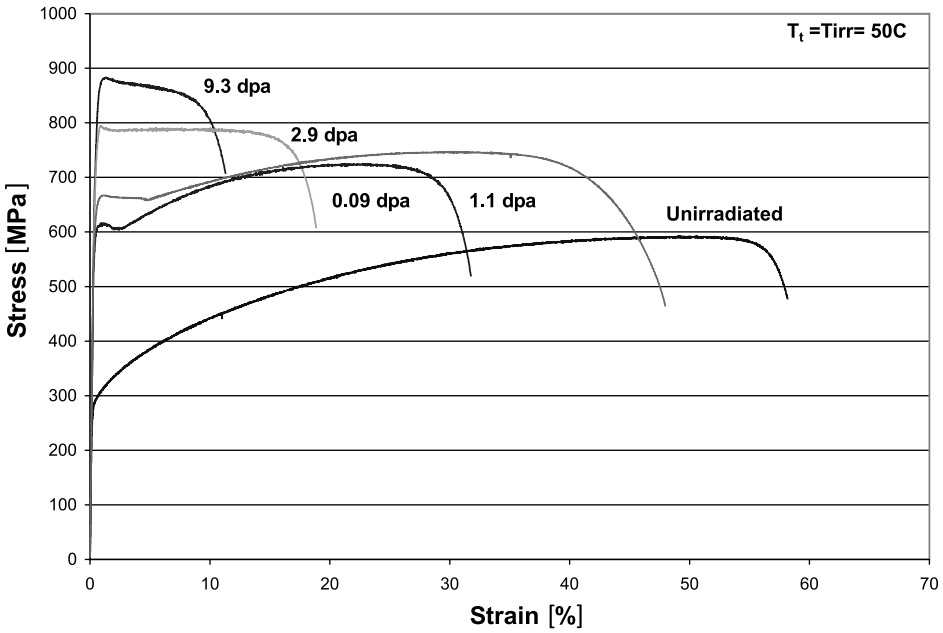

Figure 1.2: A representative stress-strain plot showing irradiation hardening for low-carbon austenitic stainless steel, 316L, as measured on annealed steel after irradiation in a spallation environment. The increase in yield stress induced in radiation-exposed materials is caused by dislocation motion being impeded by microstructures formed during irradiation. (The figure was taken from [1])

Chapter 2

Background

Section 2.1 gives a short introduction into the field of scientific computing: the advent of the "experiment on the computer", a summary on the materials simulation advances that have enabled the research presented in this report, and a short presentation on some aspects of molecular dynamics simulations. Section 2.2 attempts to summarize some basics of dislocation theory, focusing mainly on mobile dislocations, stacking faults, partial dislocations and some continuum theory.

2.1 Scientific Computing

Computer experiments play a very important role in science today. In the past, physical sciences were characterized by an interplay between experiment and theory. In experiment, a system is subjected to measurements, and results, expressed in numeric form, are obtained. In theory, a model of the system is constructed, usually in the form of a set of mathematical equations. The model is then validated by its ability to describe the system behavior in a few selected cases, simple enough to allow a solution to be computed from the equations. Unfortunately, many physical problems of extreme interest (both academic and practical) fall outside the realm of the "special circumstances" needed for typical model simplifications. Among them, one could mention the physics and chemistry of defects, surfaces, clusters of atoms and organic molecules, accurate treatment of temperature effects, disordered systems in general and so on.

The advent of high speed computers altered the picture by inserting a new element right in between experiment and theory: the computer experiment. In a computer experiment, a model is still provided by theorists, but the calculations are carried out by the machine by following an algorithm,

implemented in a suitable programming language. In this way, complexity can be introduced and more realistic systems can be investigated, opening a road towards a better understanding of real experiments.

Needless to say, the development of computer experiments altered substantially the traditional relationship between theory and experiment. On one side, computer simulations increased the demand for accuracy of the models. For instance, a molecular dynamics simulation allows to evaluate the melting temperature of a material, modeled by means of a certain interaction law. This is a difficult test for the theoretical model to pass - and a test which has not been available in the past. Therefore, simulation "brings to life" the models, disclosing critical areas and providing suggestions to improve them.

On the other side, simulation can often come very close to experimental conditions, to the extent that computer results can sometimes be compared directly with experimental results. When this happens, simulation becomes an extremely powerful tool not only to understand and interpret the experiments at the microscopic level, but also to study regions which are not accessible experimentally, or which would imply very expensive experiments.

Last but not least, computer simulations allow thought experiments, things which are just impossible to do in reality, but whose outcome greatly increases our understanding of phenomena, to be realized. [8, 9]

2.1.1 Simulation of Materials

Fast development of computer power and the growing need for predictive models in materials science have created a computational-based investigative approach called multiscale materials modeling. In this, the main goal is to understand and predict the behavior of materials under different physical and thermal conditions across all relevant time and length scales by coupling different theoretical and computational techniques. From the smallest time and length scale to the largest, the techniques involved can range from first-principles electronic calculations to large-scale classical atomic modeling (molecular dynamics (MD) and statics (MS)) to Monte Carlo simulations to continuum (elasticity theory and rate theory) calculations to large-scale finite element modeling. Each technique has a limited range of applicability but information gained from fine-scale calculations can provide data and mechanisms for coarser-scale models.

One of the most important interfaces lies between the atomic and continuum scales. Continuum elasticity theory has been developed successfully for many decades and a general picture of the mechanical response of materials has been obtained. On the other hand, there are obvious problems in treating

processes within continuum theory that are controlled by atomic-scale mechanisms. Examples include dislocation core structure, dislocation-obstacle interactions and temperature effects. Such problems can in principle be studied via atomic modeling techniques, and the important question is how the atomic and continuum approaches can be overlapped within the same scale to be mutually validated. This is not a trivial task, the main problem arising from the need to simulate large enough length and timescales in atomic modeling, e.g. lengths of the order of the distance between dislocations and times of the order of dislocation-obstacle interactions under reasonable rates of deformation.

It is more than 40 years since atomic-level models were used for dislocations, and three qualitatively different groups of methods are available [10]. One of these techniques, the one most relevant to this report, arises from modeling a periodic array of dislocations (PAD) and is based on an approach proposed by Daw and Baskes 1989, [11]. The main idea is to simulate a crystal containing an edge dislocation and apply periodic boundary conditions along not only the dislocation line but also the direction of the Burgers vector b. Models based on a PAD are very simple from the computational point of view and may be applied to simulate long (in principle infinite) distance motion of a dislocation at non-zero temperature. Only small modifications are needed in order to facilitate the use of screw dislocations instead of edge dislocations. Several studies of dislocation dynamics in perfect and imperfect crystals have confirmed at least the qualitative advantages of this method for investigating the atomic-level details of edge dislocation dynamics. (The above summary is a modified version of the summary found in [10].)

The development of interatomic potentials is one example of the advances in accurate and fast simulation of materials. In the past, interactions were obtained by two-body potentials with simple analytical form, such as Morse or Lennard-Jones. Today, the most accurate potentials contain many-body terms and are determined numerically by reproducing as closely as possible forces predicted by first-principle methods. We have thus moved up one level in the degree of reductionism contained in the potential since the previous generation, now limited only to the selection of its analytical form. This leads to better realism, which in turn allows for the investigation of physics problems which require a level of accuracy in the model that could not be achieved before. These new potentials could not exist without simulation: simulation is not only a link between experiment and theory, it is also a powerful tool to propel progress in new directions. [8, 9]

2.1.2 The Molecular Dynamics simulation method

Molecular Dynamics (MD) is a method of computational physics which allows to study properties and behavior of complex systems like gases, liquids and solids by calculating the motion of every particle in the system over a given time. Work flow for typical MD simulation software is illustrated in Figure 2.1. Typical examples of input to and output from such a simulated system is displayed in Figure 2.2. While the atomistic idea to solve the many-body problem numerically following Newton's equations is not exactly new, the wide range of applications and systems approachable by MD has gained new attention with the availability of modern powerful computers. On one hand, MD aids fundamental studies of statistical physics concerning, e.g., kinetic theory, fluid dynamics, transport theory or phase transitions by providing an "experiment on the computer". On the other hand, more applicative scenarios in material sciences, polymer physics, biology or chemistry are also feasible by means of MD.

Since MD is a rather straight-forward method that - for a defined interaction - does not rely on simplifications or an abstracted model, there are also limitations of this method that come along with the advantages. Because of the limited computer memory, calculation speed and time one is willing to wait for the result, systems accessible by MD are limited in size (typically $10^6 - 10^8$ particles as of 2012) and time (typically pico- or nano-seconds).

In molecular dynamics the laws of classical mechanics are followed, with Newton‘s second as the foundation:

$$\vec{F}_i = m_i \vec{a}_i \tag{2.1}$$

for each atom i in a system constituted by N atoms. Here, m_i is the atom mass, $\vec{a}_i = d^2\vec{r}_i/dt^2$ its acceleration and $\vec{F}_i$ the force acting upon it due to the interaction with other atoms. In this sense, and in contrast with the statistics-based Monte Carlo method, molecular dynamics is a deterministic technique: given an initial set of positions and velocities for the the atoms involved, the subsequent time evolution is *in principle* completely determined. In practice, the finiteness of the integration time step and arithmetic rounding errors will eventually cause the computed trajectory to deviate from the true trajectory. [9]

In order to avoid edge and wall effects on an atomistic system, it is possible to utilize *periodic boundary conditions*. Simply put, this involves putting the particles of a system into a shape which is treated as if it is surrounded by identical translated images of itself. Particles moving out on one side of that shape are trans-located back to the opposite side, and short ranged pair

forces are only considered for the closest duplicate image of every pair of particles.

2.1.2.1 Interatomic Potentials

Due to the complex nature of potential energy functions, there is no analytical solution to the integration of Newtons equation. Thus, time integration algorithms must be used for the simulation of materials. The potential energy function chosen therefore plays an important role in MD simulation: It determines both the accuracy and the computational speed. In spite of greatly increased computer speeds, the application of ab-initio methods for an atomistic simulation of materials is still limited to relatively small ensembles of atoms and, in MD, relatively short simulation times. In contrast, the use of empirical or semi empirical interatomic potentials makes it possible to simulate much larger systems, up to $10^7 - 10^8$ atoms for much longer times, and thus to tackle such problems as plastic deformation, fracture, or atomic diffusion.

For calculations involving solid metals and alloys, it is well known that pair potential functions like the typical Lennard-Jones and Morse potentials are far from satisfactory when the system is not a perfect crystal. Once surface or interface defects are included, pair potential functions that are independent of coordination cannot reproduce a realistic potential field. The *Embedded Atom Method* (EAM) was suggested and developed by Daw and Baskes [11] as a way to overcome the main problem with two-body potentials. The basic concept for EAM is that the potential energy can be calculated by embedding each atom to the electric field made of all other atoms. It should be noted that ideas of electron density and density functional theory (DFT) are discussed in the formulation of the EAM, however, they are classical potential functions and no quantum dynamics equation is solved when using the potential functions.

In EAM, the total energy of an elemental system is represented as [11]:

$$E_{tot} = \frac{1}{2} \sum_{ij} V(r_{ij}) + \sum_{i} F(\bar{\rho}_i). \tag{2.2}$$

Here $V(r_{ij})$ is a pair potential as a function of the distance r_{ij} between atoms i and j, and F is the embedding energy as a function of the host electronic density $\bar{\rho}_i$ induced at site i by all other atoms in the system. The latter is given by:

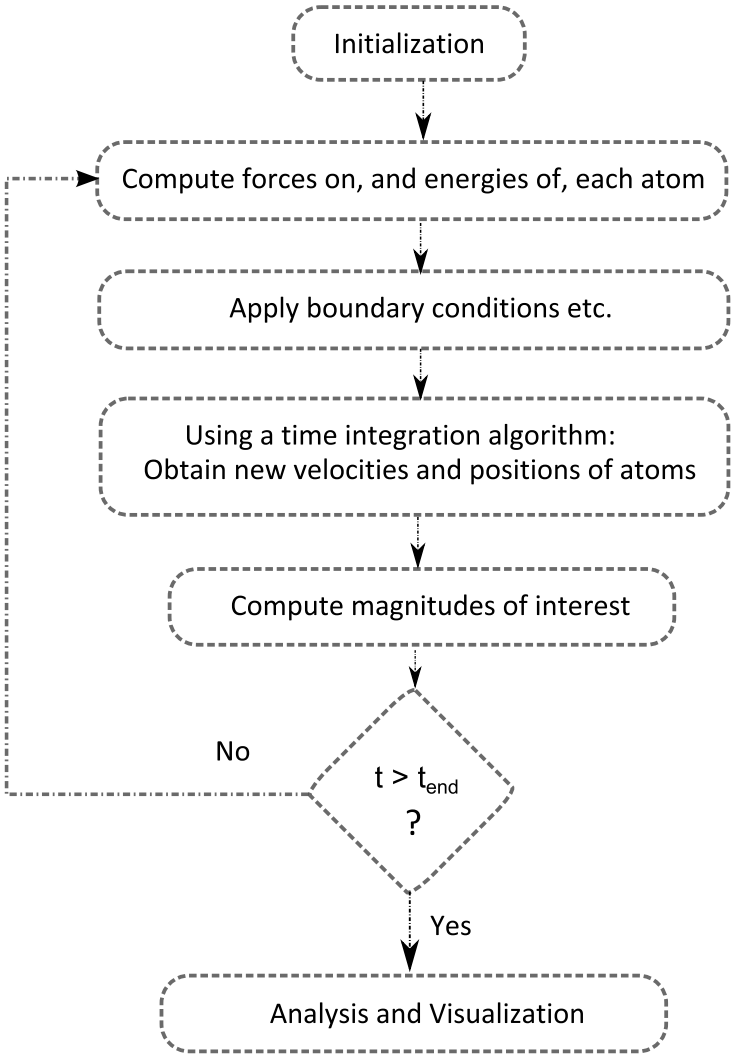

Figure 2.1: Work flow for typical MD simulation software.

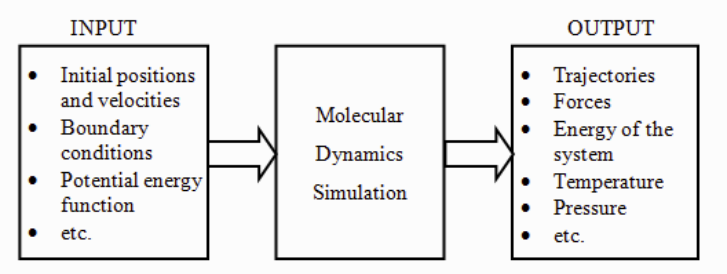

Figure 2.2: Examples of input and output for a typical MD simulation.

$$\bar{\rho}_i = \sum_{j \neq i} \rho(r_{ij}), \tag{2.3}$$

$\rho(r_{ij})$ being the "atomic density" function. The second term in 2.2 is volume dependent and represents, in an approximate manner, many-body interactions in the system. EAM potentials, together with some other similar potentials, are often referred to collectively as "glue model" potentials. All glue model potentials share the same general form given by 2.2 and 2.3, and only differ in the functional forms of $V(r)$, $\rho(r)$, and $F(\bar{\rho})$.

2.1.2.2 LAMMPS

As MD is an established method, there are existing, highly developed MD simulation programs. The program used for all simulations in this thesis is LAMMPS [12, 13], the "Large-scale Atomic/Molecular Massive Parallel Simulator". It is a classical molecular dynamics code that models an ensemble of particles in a liquid, solid, or gaseous state. The software is written in the programming language C++, and it is freely available under the GNU Public License. LAMMPS is distributed by Sandia Laboratories (USA). In 2009 alone more than 250 scientific papers referred to LAMMPS in their quotations, making it *de facto* one of the standard MD simulators.

In the most general sense, LAMMPS integrates Newton's equations of motion for collections of atoms, molecules, or macroscopic particles that interact via short- or long-range forces with a variety of initial and/or boundary conditions. It can model atomic, polymeric, biological, metallic, granular, and coarse-grained systems using a variety of force fields and boundary conditions. It can be used to model atoms or, more generically, as a parallel particle simulator at the atomic, meso, or continuum scale. LAMMPS can model systems with only a few particles up to millions or billions. LAMMPS is open-source and free, which makes it attractive for use in academic work.

LAMMPS does not require to compile own code for different MD scenarios and has instead invented a scripting language to describe settings (e.g. concerning neighbor lists), initial configurations (like atom positions, geometrical sizes and periodicity), algorithms to be computed (including force and integration algorithms), what data to output (like positions, velocities, pressure or temperature) and when to do so. LAMMPS is able to use a single processor as well as multi-core processors or multiple PCs, linked through an Ethernet network.

Parallelization

To overcome the limited memory and calculation speed available to one processor, many MD programs are designed to be parallelizable. In the case of the software used in this thesis, LAMMPS, the processes running in parallel normally execute on independent memory and need to communicate data and results among themselves. This communication based parallelization is very common. The simplest way for such communication is data replication, i.e. to copy all data to every processor (and processor core). Obviously, this requires a lot of memory and communication time. Therefore, one tries to find a way for data partitioning which aims at providing every processor only with the minimum data it needs for the calculation. In the case of short-range potentials, one such method is spatial decomposition, which geometrically divides the whole simulation area into sub-domains (cells). That way, every processor only needs to be aware of the particles of its own cell and the particles close to the border of the neighboring cells. Communication is limited to the particles moving in and out of a cell and possible forces acting on border particles. LAMMPS uses this paradigm, and it actually originates from an effort to do this spatial decomposition in an effective manner based on the work by Steve Plimpton in "Fast Parallel Algorithms for Short - Range Molecular Dynamics" [12].

Visualization of simulations: AtomEye

Visualization of simulation results plays the same role as microscopy in experiments: we rely on it to extract mechanistic information, before we decide what to do next (more calculations or experiments) to accentuate a certain finding or theory. In this feedback, the capabilities and ease-of-use of the visualization software employed are actually important towards scientific discovery, even though one may initially consider it as merely a technical detail.

AtomEye [14] is free atomistic visualization software for all major UNIX platforms. It is based on an independently developed graphics core library of higher quality than the X-window standard, with area-weighted anti-aliasing. AtomEye has been used actively in the research leading to this report, and all figures displaying spherical atoms in this report are exported from AtomEye. The program is efficient compared to Open GL hardware acceleration by employing special algorithms to treat spheres (atoms) and cylinders (bonds), in which they are rendered as primitive objects rather than as composites of polygons.

2.2 Dislocation Theory

The smelting and forging of metals marks the beginning of civilization - the art of working metals was for thousands of years the major "high tech" industry of our ancestors. However, exactly *why* metals could be plastically deformed, and why the plastic deformation properties could be changed to a very large degree by forging without changing the chemical composition, was a mystery for thousands of years. No explanation was offered before 1934 - this section will give a short introduction to the fundamental discoveries that since followed. The subject of dislocations is essential for an understanding of many of the physical and mechanical properties of crystalline solids. Although there are many techniques now available for the direct observation of dislocations, the existence of these line defects was deduced by inference in the early stages of dislocation study in the thirties, forties and fifties.

The shear stress required for plastic deformation of a single crystal was first calculated by Frenkel in 1926. He assumed that deformation would occur in such a crystal through atomic planes sliding over each other, requiring a rigid co-operative movement of all the atoms from one position of perfect registry to another. His work resulted in a sinusoidal relation describing the shearing force required for this movement. The maximum value of this shearing force is the *theoretical critical shear stress*. The values obtained for this shear stress were several orders of magnitude greater than the observed experimental values however, and it was clear that some mechanisms were unaccounted for.

An explanation was worked out independently by Orowan, Polanyi and Taylor in 1934. They suggested the presence of *dislocations*, a crystallographic defect, or irregularity, within a crystal structure. Dislocation densities in actual crystals depend on the preparation of the specimen, but can range from 10^2 to 10^{12} $1/\text{cm}^2$. There are two primary dislocation types: edge dislocations and screw dislocations. Mixed dislocations are intermediates between these.

Figure 2.3 illustrates the two primary types of dislocations. One can imagine constructing an edge dislocation (Figure 2.3(a)) by removing or adding a half plane of atoms to a crystal which is terminating in the dislocation line, and then carefully joining back together the two planes on either side of the missing plane in a way that restores the basic order of the perfect crystal everywhere except in the vicinity of the dislocation line. Similarly, a screw dislocation (Figure 2.3(b)) can be constructed by imagining a plane terminating at the dislocation line, above which the crystal has been displaced by a lattice vector parallel to the line, and then rejoined to the part of the crystal below in a way that preserves the basic crystalline order everywhere

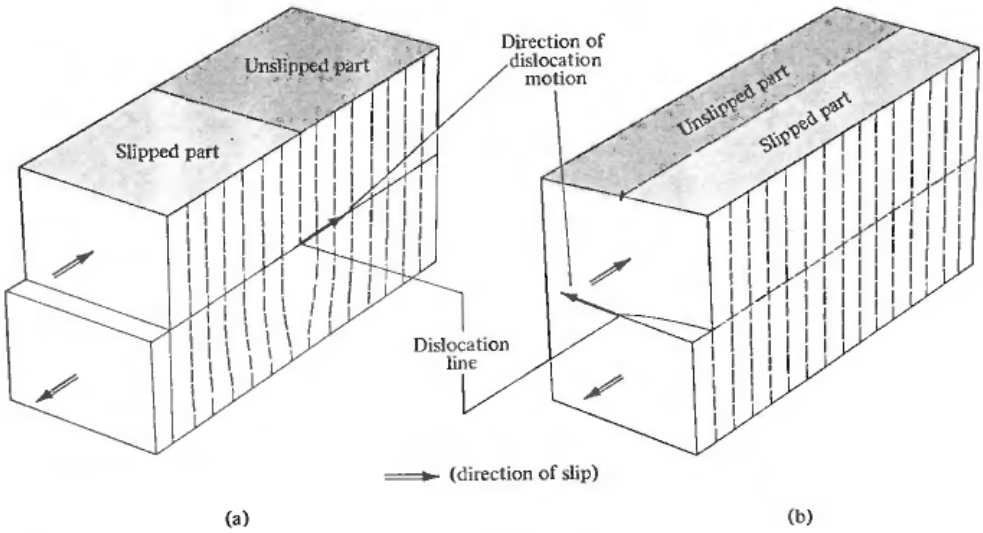

Figure 2.3: (a) Slip in a crystal via the motion of an edge dislocation. (b) Slip in a crystal via the motion of a screw dislocation. [15].

except near the line itself. [15]

Along a linear dislocation the crystal is in so high a state of local distortion that the additional force required to move the dislocation sideways by one lattice constant requires relatively little additional applied stress. The energy required to break a single bond is far less than that required to break all the bonds on an entire plane of atoms at once. This suggests that plasticity is possible at much lower stresses than in a perfect crystal. In many materials, particularly ductile materials, dislocations are the "carriers" of plastic deformation, since the energy required to move them is less than the energy required to fracture the material. Dislocations therefore give rise to the characteristic malleability of metals. The dislocations move along the densest planes of atoms in a material, because the stress needed to move the dislocation increases with the spacing between the planes. Face-centered cubic (FCC) and body-centered cubic (BCC) metals have many dense planes, so dislocations move with relative ease and these materials therefore have high ductility. Metals are strengthened by making it more difficult for dislocations to move. This may involve the introduction of obstacles, such as interstitial atoms, voids or grain boundaries, to "pin" the dislocations. Also, as a material plastically deforms, more dislocations are produced. These will eventually get into each others way and impede movement. This causes a

hardening of the metal as deformation progresses. This effect is known as strain hardening (also work hardening).[2]

The effects of strain hardening by accumulation of dislocations can be removed by appropriate heat treatment (annealing) which promotes the recovery and subsequent recrystallization of the material. The combined processing techniques of work hardening and annealing allow for control over dislocation density, the degree of dislocation entanglement, and ultimately the yield strength of the material.

2.2.1 Stacking Faults and the Stacking Fault Energy

In the FCC structure, shown in Figure 2.4, the atoms are situated at the corners of the unit cell and at the centers of all the cube faces in sites of the type $0,\frac{1}{2},\frac{1}{2}$. The atoms touch along the <011> close-packed directions. The lattice parameter $a = {}^{4r}/\sqrt{2}$. The stacking sequence of {100} and {110} planes is ABABAB... , and the stacking sequence of {111} planes is ABCABC... The latter is of considerable importance and is illustrated in Figure 2.4. The atoms in the {111} planes are in the most close-packed arrangement possible for spheres and contain three <110> close-packed directions 60^{o} apart.

All real crystals contain imperfections which may be point, line, surface or volume defects, and which disturb locally the regular arrangement of the atoms. A stacking fault is a planar defect, a local region in a crystal where the regular stacking sequence has been interrupted. Stacking faults destroy the perfection of the host crystal, and the associated energy per unit area of fault is known as the stacking-fault energy. Typical values lie in the range 1-1000 mJ/m^2. A stacking fault in FCC material amounts to a layer of hexagonal symmetry approximately three or four atomic planes thick. For stacking of the close-packed planes in close-packed structures there are two possible positions of one layer resting on another (Figure 2.4). According to the hard sphere model, a close-packed layer of atoms resting on an A layer can rest equally well in either a B or a C position and geometrically there is no reason for the selection of a particular position. In a face-centered cubic lattice two types of stacking fault are possible, referred to as intrinsic and extrinsic. These are best described by considering the change in sequence resulting from the removal or introduction of an extra layer. [2]

An FCC metal of low stability with respect to the hexagonal close packed atomic arrangement will have a low stacking fault energy. Austenitic Stainless Steel, an FCC material, have occupied a central place in this interest, and its stacking-fault energy was one of the first to be measured. The SFE of stainless steels, and especially austenitic stainless steels, are very low. This

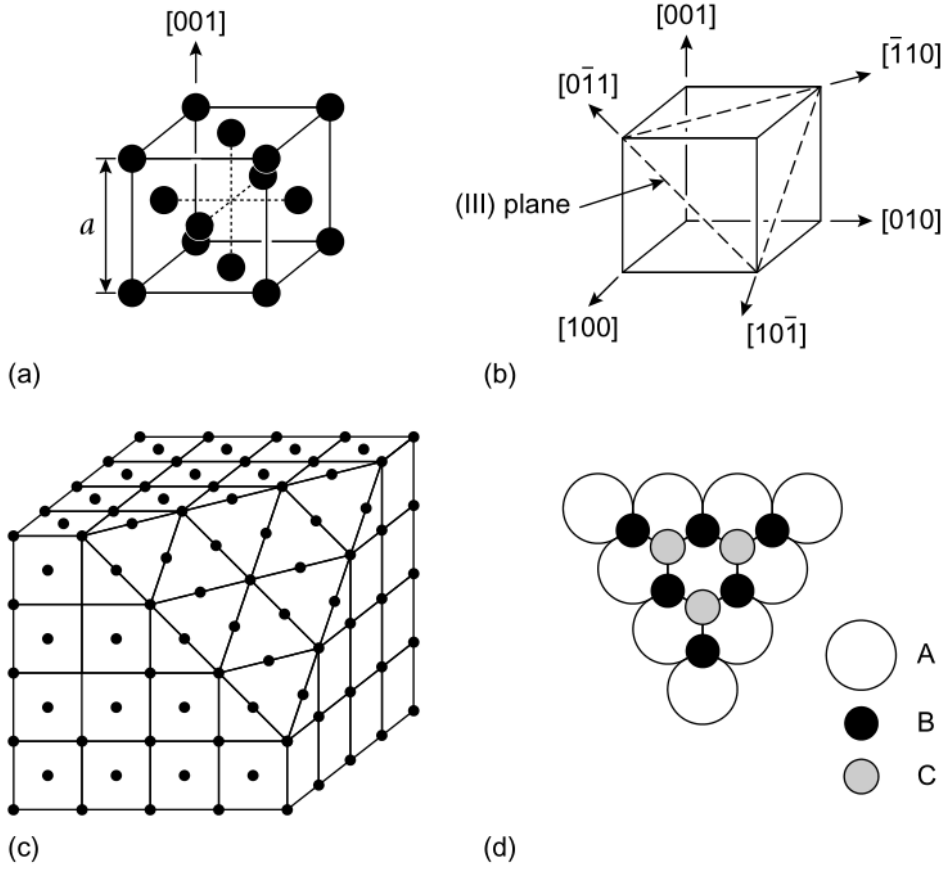

Figure 2.4: Face-centered cubic structure: (a) unit cell, (b) principal directions, (c) arrangement of atoms in a (111) close-packed plane, (d) stacking sequence of {111} planes. [2]

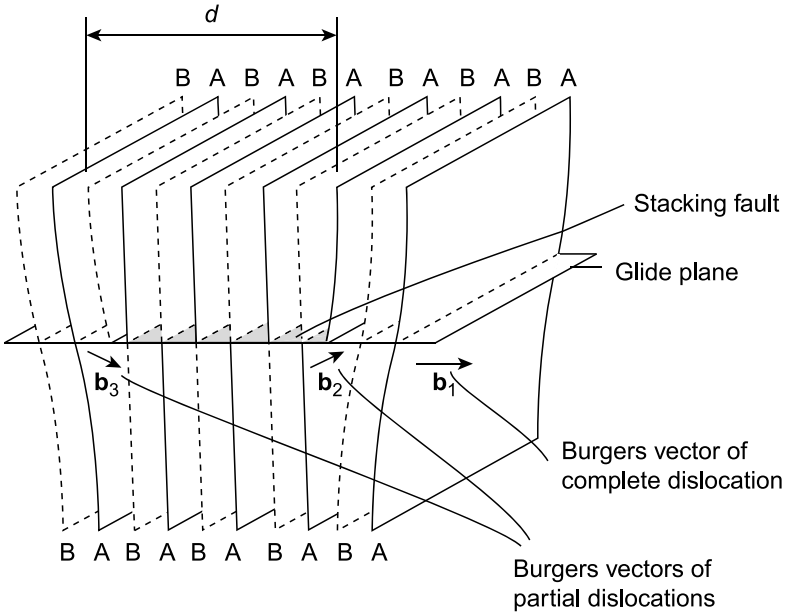

Figure 2.5: Formation of an extended dislocation by dissociation of a unit edge dislocation into two Shockley partials of Burgers vectors $b_2$and $b_3$separated by a stacking fault. The labels ABAB... refer to the stacking of (110) planes. [2]

material was by the end of the 1950s known to twin easily and to transform partially into a hexagonal phase on deformation; these two facts made scientists expect the stacking fault energy to be very low, which was confirmed by Whelan, Hirsch, Horne and Bollmann in 1957 [16]. They confirmed experimentally the relatively new theory that the dislocations in stainless steel can split into partial dislocations, and found that the low stacking fault energy lead to wide stacking faults between the Shockley partials. The observations were concluded to be in absolute contrast to those made on aluminum, a metal of high SFE.

Stacking fault energy is usually measured in [mJ/m^2] or [meV/$\mathring{A}^2$], but can also be described as a force per unit length: [N/m]. Stacking fault energy is heavily influenced by a few major factors, specifically base metal, alloying metals, percent of alloy metals, and valence-electron to atom ratio. We will continue discussing the influence and importance of SFE in the next section.

2.2.2 Partial Dislocations: the Shockley Partial

Partial dislocations are important in twinning reactions, in phase transformations, and in the formation of dislocation barriers by intersecting dislocations. The extension of a perfect dislocation into dislocation partials bounding a stacking fault affects the climb and cross slip of dislocations. Stacking faults themselves are important barriers to dislocation motion.

It was Heidenreich & Shockley[17] who in 1948 suggested that a dislocation in a FCC lattice may dissociate into two partial dislocations according to the reaction [16]:

$$\vec{b_1} \rightarrow \vec{b_2} + \vec{b_3} \tag{2.4}$$

or

$$\frac{1}{2}a[\bar{1}10] = \frac{1}{6}a[\bar{2}11] + \frac{1}{6}a[\bar{1}2\dot{1}]. \tag{2.5}$$

Both of these partials are glissile in the (111) plane. This splitting reaction can be shown to be energetically favorable according to the Frank criterion: $b_1^2 = {}^{a^2}/_2$, the energy contained by the perfect dislocation, is greater than $b_2^2 + b_3^2 = {}^{a^2}/_3$, the energy contained by the two partial dislocations[2]. The partials repel each other, leaving a ribbon of stacking fault between them. This repulsion is a result of the elastic interactions that follow their 60° orientation difference. The equilibrium distance between these two partial dislocations, and thereby the width of the stacking fault, is given by the balance between the repulsive force of the partials themselves and the attractive force due to the surface tension of the stacking fault. The SFE indicates this equilibrium distance through these relationships [2]:

$$d_{eq} = \frac{Ga^2}{16\pi}\left\{\frac{2+\nu}{3\,(1-\nu)}\right\}\frac{1}{\Gamma_{SFE}}\ \text{(edge)} \tag{2.6}$$

$$d_{eq} = \frac{Ga^2}{16\pi}\left\{\frac{2-3\nu}{3\,(1-\nu)}\right\}\frac{1}{\Gamma_{SFE}}\ \text{(screw)} \tag{2.7}$$

Where G is the shear stress, a is the lattice parameter and ν is the Poisson ratio. This configuration, illustrated as a general case in Figure 2.6, is called an extended dislocation. The stacking sequence of {111} planes outside the dislocation will be ABCABCABC... as in standard FCC, but between the partial dislocations it will be ABCACABC... This is an intrinsic stacking fault, equivalent to four layers of close-packed hexagonal stacking. During glide under stress, the leading partial dislocation will be creating the fault

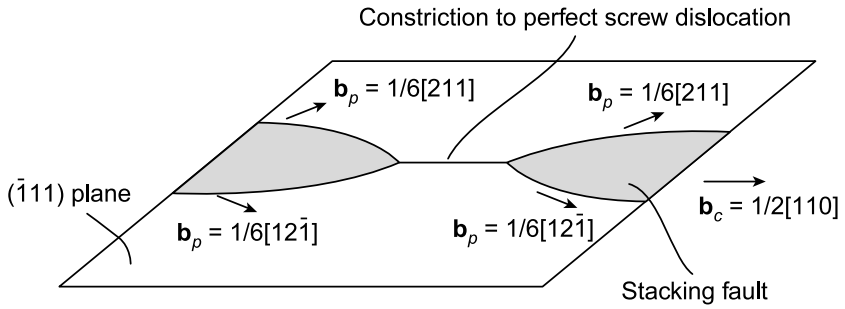

Figure 2.6: Constriction to a perfect screw segment in an extended dislocation in a face-centered cubic metal.The Burgers vector of a Shockley partial is denoted by b_p, that of the perfect screw by b_c. [2]

and the trailing one will be removing it. Note that the width, d_{eq}, is inversely proportional to the stacking fault energy. This width is however the only difference between the dissociation of dislocations of different character (edge, screw, mixed). Some theoretical predictions for this separation distance, from Equation 2.6, can be seen in Figure 2.8. Dislocation lines in aluminum are clearly not appreciably extended, in contrast to the case of copper or austenitic stainless steel. These differences in stacking-fault energy and ribbon width are thought to account largely for the differences in mechanical properties between the different face-centered cubic metals. For example, the SFE modifies the ability of a dislocation in a crystal to glide onto an intersecting slip plane. It is important to note that the shear modulus (G, μ) for ASS is twice that of Cu, increasing the separation distance between partials accordingly. [16]

The *cross-slip process*, through which screw dislocations move from one slip plane to another with relative ease, is a fundamental factor in the technological utility of metals which crystallize in the FCC structure. The sequence of events envisaged during the cross-slip process for dissociated dislocations in FCC materials is illustrated in Figure 2.7. A dissociated dislocation, lying in the (111) slip plane in (a), has been constricted along a short length in (b). The constricted dislocation has a pure screw orientation and is therefore unstable with respect to redissociation. A constriction is likely to form at a barrier provided by a non-glissile dislocation or impenetrable particle, as the voids discussed in this thesis, where the applied stress tends to push the partials together. By stage (c) the unit dislocation has dissociated into two different partial dislocations with a stacking fault but on the (11$\bar{1}$) plane rather than (111). The new extended dislocation is free to glide in the cross-

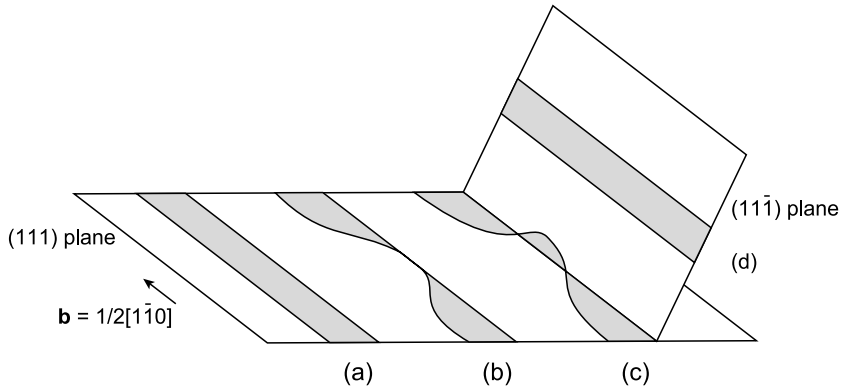

Figure 2.7: Four stages in the cross slip of a dissociated dislocation (a) by the formation of a constricted screw segment (b). The screw has dissociated in the cross-slip plane at (c). [2]

slip plane and has transferred totally to this plane by stage (d).[2, 18]

2.2.3 Continuum theory

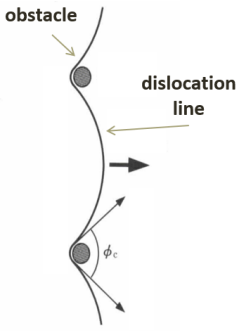

Orowan Model

The pivotal role of dislocations in the plasticity of metals is apparent at length scales ranging from the very long (micrometres), for which analytic linear elastic continuum theory is well developed, to the very short (nanometres), at which recourse must be had to numerical atomistic methods. We will in the following summarize some relevant theory and equations based in analytic linear elastic continuum theory.

The flow stress resulting from a distribution of impenetrable obstacles on the slip plane was first treated by Orowan in 1948. Considering a dislocation bowing between an isolated pair of such obstacles, and using a constant line tension approximation, he derived a relation for the flow stress (denoted Orowan stress): $\tau_{Orowan} \approx \frac{Gb}{L}$, where G, L, and b are the shear modulus, spacing between obstacles, and the Burgers vector, respectively.

For a periodic array of obstacles whose spacing is L, the Critical Resolved Shear Stress (CRSS) above which a dislocation can penetrate the array of obstacles is often represented by:

$$\tau_c = \frac{2\gamma}{bL} \cos \frac{\phi_c}{2}, \tag{2.8}$$

where b denotes the Burgers vector length of a dislocation, γ is the dislocation line tension, L is the obstacle spacing and ϕ_c is the critical angle

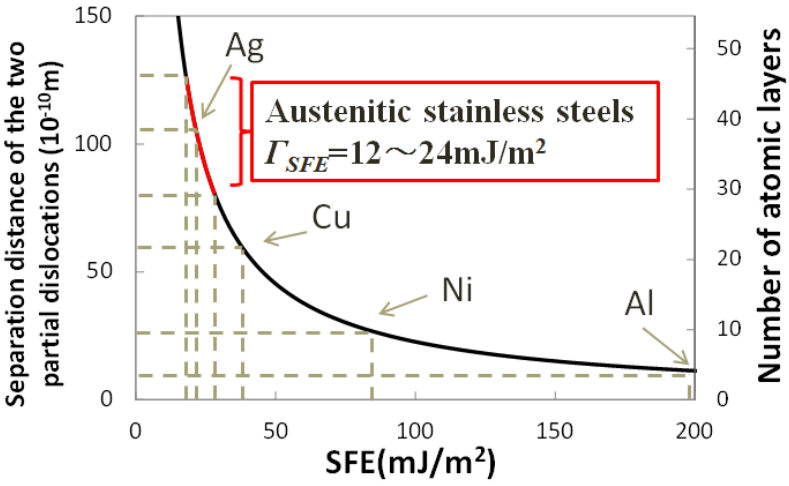

Figure 2.8: Equilibrium separation distance between two Shockley partials as a function of Stacking Fault Energy (SFE). Calculated using Equation 2.6.

at dislocation breakaway (depinning). This model is assuming constant line tension. The line tension γ is given by elasticity theory and is often written as $Gb^2/2$, where G represents the shear modulus.

Improved formulations of this relation have later been published, and extensive experimental investigations and theoretical models of hardening can be found in the literature. As well as analytical approaches, computer simulations to investigate the interaction of dislocations with different obstacles were first performed using the discrete dislocation model. The latter emerged from the pioneering work of Foreman and Makin [19], Kocks [20] and Scattergood and Bacon [21]in the 1970s, where dislocations were described as a connected set of straight segments. These first refinements also accounts for the effect of non-regular distribution of obstacles via the concept of an effective obstacle spacing, and can be considered as the ancestors of the dislocation dynamics (DD) models that are now highly efficient at modeling multi-dislocation dynamics on the microscopic scale, i.e. inside a grain of metal. At this time, elastic field screening which imposes a logarithmic dependency of dislocation line energy and the effect of precipitate finite size were studied respectively by Hirsch and Humphreys [22] and Scattergood, Kocks and Bacon [23]. Despite these long-standing efforts, the quantitative prediction of strengthening remains an open problem in many materials.

On the basis of their computational results from a DD model, Bacon, Kocks and Scattergood (BKS) [23] established an analytical model where the critical resolved shear stress (CRSS) required for an edge dislocation to

bypass a regular array of non-penetrable inclusions can be written as:

$$\tau_c = \frac{Gb}{2\pi L\,(1-\nu)}\left[\ln\left(\frac{1}{(0.5r^{-1}+L^{-1})}\right)+B\right] \tag{2.9}$$

where G, L, and ν are the shear modulus, spacing between obstacles, and the Poisson ratio, respectively. The Poisson ratio is set to zero for edge dislocations, and equals approximately 1/3 for screw dislocations in Cu.B is an adjustable parameter which can be related to the inner cutoff radius$q$ of elastic theory [15]; throughout $B = -\ln(q)$. The latter relation is intended to represent the dislocation core contribution, with q on the same order as the Burgers vector length. The BKS theory implies several approximations, thoroughly described in the original BKS paper [23] and various improvements have also been proposed [10, 24, 5, 6, 7, 25].

Dissociation of dislocations into Shockley partials is not taken into account in the BKS model, so it is expected to be more accurate for cases of simultaneous dislocation release from obstacles.

It is energetically favorable for a dislocation to intersect a void because its core and strain energy is zero within the cavity. However, the dislocation has to create a surface step (in the direction of its Burgers vector b) by shear as it cuts a void. These two effects determine the magnitude of the applied stress that is necessary for the dislocation to break away, but are not easily modeled using elasticity theory [21, 5].

Chapter 3

Method and Model

3.1 General Model

Nanoscale interactions between a moving dissociated edge/screw dislocation and voids have been studied using PAD (Section 2.1.1) models, applied for dynamic ($T > 0$ K) conditions. We have used the LAMMPS [12, 13] molecular dynamics code, described in Section 2.1.2.2. The highly refined *Embedded Atom Technique* (EAM) was utilized for interatomic potentials. Current research is based on FCC copper (Cu) potentials made by Mikhail Mendelev (Ames Laboratory) [26] and Yuri Mishin [27]. Mendelev has created a set of Cu potentials with differing values of SFE, and these were used extensively in this thesis work. Some more information regarding the interatomic potentials are given in Section 3.1.1.

The atomic models used were similar to those developed in [10], used in [5, 6, 7, 24]. These models are designed to allow an initially straight, infinitely long edge or screw dislocation to glide under the action of shear loading and encounter a periodic row of obstacles, in this case voids, on its glide plane. The x, y, and z axis are taken as the $[10\bar{1}]$, $[1\bar{2}1]$, and $[111]$ directions, respectively. Periodic boundary conditions were imposed along both x and y in all cases. Rigid atom surfaces were located at $\pm z$, resulting in their surface normals being parallel with the z direction. The voids were of spherical shape, with their center on the dislocation glide plane. Crystals of different sizes were simulated in order to study the effect of void spacing, L, along the dislocation line.

The models were loaded in shear by applying shear strain ϵ_{xz}via the rigid layers of atoms on the $\pm z$ surfaces. The LAMMPS "ramp displacement" style was used to displace atoms a variable amount in the $\pm x$ directions depending on the atom's coordinate in the $\pm z$ directions. The surface atoms were fixed

in between displacement. It is common to impose a shear strain to the cell by simply locking the atoms on one surface while moving the other surface in increments, but this can lead to displacement shock waves moving through the cell. The "ramp displacement" method has the advantage of obtaining the same shear strain through a dispersed displacement throughout the cell, thereby minimizing shock effects. The displacement was done every 100 timesteps. The applied strain rate was $\dot{\epsilon} = 8 \times 10^6\,\mathrm{s}^{-1}$ in all simulations. At these strain rates, the steady state dislocation velocity varies from 20 to 500 m/s for the model sizes used. The applied shear stress, τ , corresponding to the strain was calculated from the symmetric per-atom stress tensor S_{xz} for each mobile atom in the simulation through a summation and simulation cell volume division. The Critical Resolved Shear Stress (CRSS), τ_c, was taken to be the maximum of τ immediately before the release of the dislocations from the array of voids.

Micro-canonical ("NVE") integration was set to update the position and velocity of the atoms each timestep. This creates a system trajectory consistent with the micro-canonical ensemble. Temperatures ranging from 10 to 600K were obtained through generation of a Gaussian velocity distribution throughout the simulation cell. The Gaussian distribution had a mean of 0.0 and a sigma scaled to produce the requested temperature. Molecular statics (MS), which simulate crystals at $T = 0$ K, can in many cases be easier to compare to the different elasticity models available. We have however decided to exclusively use MD, simulating systems at finite nonzero temperatures. The total simulation time varied from 1 ns to 4 ns depending on the level of shear strain needed for the dislocation to overcome the array of voids, normally between 0.8 % to 2 %. The MD timestep was set to be 20 fs in most edge dislocation simulations and 10 fs in all screw dislocation simulations. A timestep of maximum 10 fs was necessary for all simulations at system temperatures higher than 250 K. The atomic structure of the void and dislocation was stored for later inspection through AtomEye (Section 2.1.2.2) every 500 timesteps.

The Cu crystal lattice was in all cases generated by a custom-made program, separate from LAMMPS. This program first generates a perfect lattice, and then modifies this lattice to include the chosen dislocation and spherical void at their chosen coordinates. This setup of atoms is then passed on to the LAMMPS MD program. It is first relaxed to a potential energy minimum so that the perfect dislocation dissociates into two Shockley partials, and it is then heated to the chosen temperature before the straining of the cell commences.

The relevant shear modulus G calculated from the elastic constants given in the appendix for the potentials used is in the range 46 - 48 GPa. We

therefore used $G = 47$ GPa in Equation 2.9 whenever this equation was utilized in the following. We set the Poisson Ratio to $\nu = 1/3$ for screw dislocations in the same equation.

3.1.1 Interatomic Potentials

As mentioned earlier we utilize the highly refined *Embedded Atom Method* (EAM) for interatomic potentials. Mikhail Mendelev of Ames Laboratory has created a set of potentials for Cu with differing values of stacking fault energy, enabling us to investigate the *isolated influence* of SFE on dislocation dynamics in atomistic MD simulations. This has, to the authors knowledge, not been done before. Seven different potentials created by Mendelev have been used in this thesis, all similar in all respects but with differing values of SFE: 14.6, 24.9, 38.1, 44.1, 61.7, 94.7 and 186.6 mJ/m^2. The potential with a SFE of 38.1 mJ/m^2 is available to the public and is based on the research conducted in [26]. The SFE of the potential created by Yuri Mishin [27] is 44.4mJ/m^2. A detailed set of parameters describing the seven different Cu potentials created by Mendelev, and also parameters describing the Cu potential made by Mishin can be found in the appendix.

3.2 Edge Dislocation Model

A schematic of the model used for edge dislocations is shown in Fig. 3.1.The length of the x and z dimensions were 33nm and 26nm respectively, but were increased slightly for simulations involving the larger voids in order to avoid finite cell size effects. The length of the y axis and thereby also the centre-to-centre spacing of the voids, L, along the periodic row was 35.5nm in all simulations expect in those investigating the effect of changing L directly. The dislocation had its initial Burgers vector in the x direction of the model, while the initial edge dislocation core and the row of voids were parallel with the y axis. The Burgers vector and glide plane were $\frac{1}{2}[10\bar{1}]$ and (111), respectively. This Burgers vector describes one of the perfect dislocations possible in FCC. The dislocation always dissociate in its glide plane into two $\frac{1}{6}[112]$ Shockley partials, as described in Section 2.2.2.

The movement of edge dislocations may be impeded not only by interaction of the dislocation core with the void center, but also at interaction points far from the void center. Hence, we have conducted simulations for several shifted glide planes as shown in Figure 3.2.We name the shifted distance the *"impact parameter"*, denoted by x/r as a ratio between distance from void center and void radius.

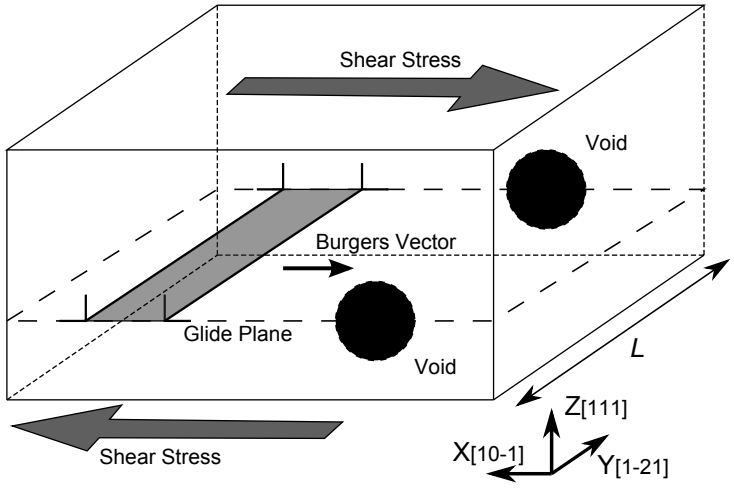

Figure 3.1: Model schematic: The edge simulation cell. Each cell contains one void only, but two half-voids are displayed here in order to better visualize the periodic boundary conditions. The area shaded in gray color represents the stacking fault, bounded by two Shockley partial dislocations. Apart from a change in orientation, this model is identical to the model visualized in Figure 3.3.

The void diameter, D, was between 1 and 8 nm. Voids in these ranges of D contain between 43 and 22 760 vacant lattice sites in Cu. As D increases, the obstacle strength of the voids increase and the dislocation bows out more before breaking away. It was therefore necessary to increase the model size along x accordingly. Values in the ranges 33 to 60 nm were used. The z dimension was 26 nm, giving the models approximately 3.5 to 5.3 million lattice sites.

The edge dislocation is created in the simulation cell by the insertion of an extra half-plane of atoms as described in Section 2.2. As previously mentioned this is not a functionality offered by the LAMMPS MD simulation software, and was therefore achieved by the use of software developed internally in the laboratory group.

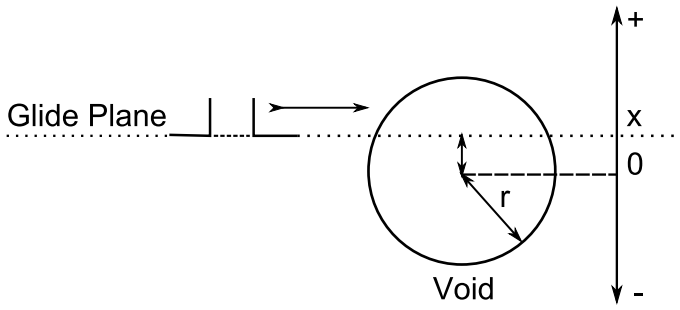

Figure 3.2: Model schematic: The Impact Parameter x/r is defined as the ratio between the distance from the void center to the glide plane divided by the radius of the void. Note that the lower part of the void corresponds to negative values of the impact parameter.

3.3 Screw Dislocation Model

The model used for the simulation of screw dislocation interactions is similar to the one used for edge dislocations. The general features of simulation are the same as previously described, but the simulation cell is slightly smaller, and the direction of glide is perpendicular relative to the model used for edge dislocations. This does not influence or compromise the simulated interactions significantly, but will be mentioned in the discussion.

The dimensions of the model system were $20 \times 29 \times 20\text{nm}^3$ for all simulations, visualized in Figure 3.3. These are the same dimensions as used by Hatano *et al.* in [7]. The length of the y axis and thereby also the centre-to-centre spacing of the voids, L, along the periodic row was kept at 20 nm in all simulations expect in those investigating the effect of varying L directly. The screw dislocation had its initial Burgers vector in the x direction of the model, and so both the initial screw dislocation core and the row of voids were parallel with the x axis. The simulated system consisted of approximately 9.2×10^5atoms.

The initial Burgers vector and glide plane were $\frac{1}{2}[10\bar{1}]$ and (111), respectively. This Burgers vector describes one of the perfect dislocations possible in FCC crystals. The dislocation always dissociate in its glide plane into two Shockley partials of mixed dislocation character, separated by a stacking fault ribbon on (111). In order to introduce a screw dislocation whose Burgers vector is parallel to the x axis, we first prepare a perfect crystal and then displace atoms by the same procedure as the one used by Hatano *et al.* in [7]. Note that we cannot adopt a periodic boundary condition with

respect to the y direction because the relative displacement of two adjacent cells is $b/2$. Thus, a modified periodic boundary condition is adopted, under which the adjacent cells are displaced by $b/2$ along the x direction. As to the x direction, an ordinary periodic boundary condition is employed so that we consider a screw dislocation of infinite length. Note also that the surfaces exist only in the $\pm z$ directions, as in the edge dislocation model. A void is introduced by removing atoms that belong to a spherical region whose radius is r.

The void diameter, D, was varied between 1 and 6 nm. Voids in this range of D contain between 43 and 15 000 vacant lattice sites in Cu. As D increases, the obstacle strength of voids increase and the dislocation bows out more before breaking away.

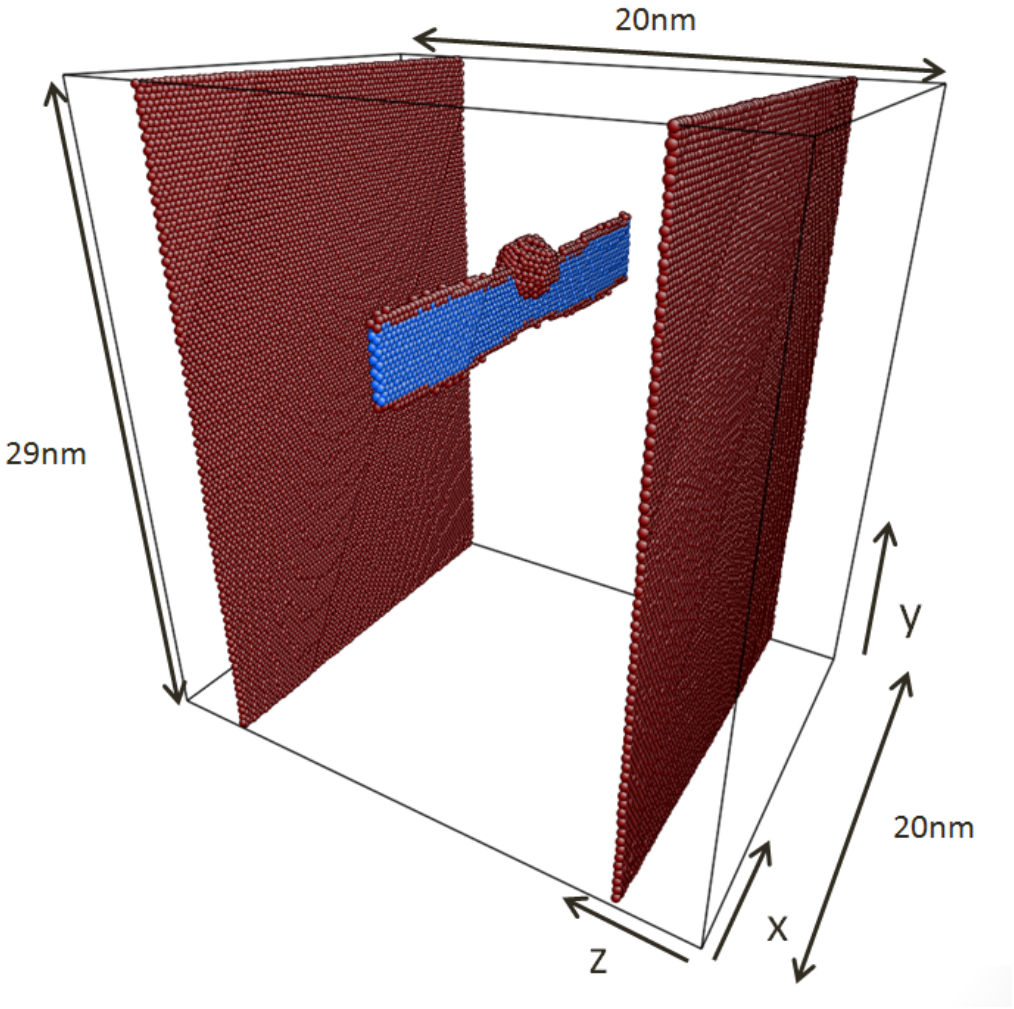

Figure 3.3: Screw dislocation model, as visualized by AtomEye through common neighbor analysis. Only atoms with a non-standard FCC crystal lattice position are visible, in addition to the surface layer of atoms. The surface atoms of the void and the partial dislocation cores are shown in red color. The atoms central in the stacking fault bounded by the partials are colored blue. One partial is seen to be pinned on the void surface. Apart from a change in orientation this model is identical to Figure 3.1, and should be supplemented with model information from that figure.

Chapter 4

Results and Discussion

This chapter will describe the actual results obtained through molecular dynamics simulations. We will first focus on the behavior of the edge dislocation interactions, and then secondly on the screw dislocation interactions. The general behavior of the two types of dislocations are similar, but the edge dislocation is generally simpler and more predictable. It will therefore serve as an introduction to the more challenging screw dislocation interactions. Some general aspects of dislocation - void interaction mechanics will therefore be explained only for edge dislocations.

Different simulations based on identical conditions always give slightly different values for the critical shear stress because of the stochastic nature of the unpinning process. All results presented are therefore averaged over multiple simulations, run with velocity distributions based on a random seed. All results are verified not to deviate from the presented values in such a way that it effects the conclusions based on the results. Error bars are not included in the presented results, but an uncertainty of approx. 10 % must be expected in most cases. Fluctuations in shear stress make it challenging to record the accurate critical stress at dislocation release from the voids

The temperature of the simulated systems were verified for all simulations to be within $\pm$5K of the set temperature throughout the simulations, implying that constant temperature conditions and energy conservation were well satisfied.

4.1 The Edge Dislocation

We will in this section focus on the simulation results obtained with an initially straight edge dislocation and its interaction with an infinite array of voids in its glide path. The originally perfect dislocation dissociates into two Shockley partials in all simulations regardless of interatomic potential, but with an equilibrium separation distance according to the intrinsic stacking fault energy of the potential selected for the simulation. It is clear that the value of stacking fault energy affects many aspects of the dislocation – void interaction. For edge dislocations this influence will be seen to be is rather weak but systematic.

The size and shape of a void after an interaction with a dislocation can be of critical importance to phenomenon such as dislocation channeling and the localization of plastic flow. All voids in Cu are however *simply sheared* by the passing of edge dislocations without any defect absorption, in contrast to interactions in BCC iron where the dislocation always absorbs some vacancies as observed in [24]. Multiple collisions between edge dislocations and voids have been observed in the current thesis work for some simulations as a consequence of the periodic boundary conditions. This secondary pinning on the void leads to CRSS values of similar value to the first pinning interaction, and simply increases the shear of the voids, as noted in [6]. The value of SFE does not seem to affect this mechanism, and this subject will therefore not be discussed further in the following.

4.1.1 Description of General Interaction Behavior

A typical interaction process between a periodic array of voids and a dissociated edge dislocation is illustrated in Figure 4.1. Plots of shear stress,τ, versus applied strain,ϵ, for an edge dislocation - void interaction at two different values of SFE are presented in Figure 4.2, starting from the initial state when the straight dislocation is outside the row of voids. The plots contain distinct regions that are similar to all simulation results of this kind: (i) The dislocation glides towards the void when τ reaches the Peierls stress. (ii) It is then attracted by, and pulled into, the void. τ now decrease, often to a net negative value, because the plastic shear strain due to dislocation motion is larger than the imposed strain. As mentioned in Section 2.2.3, it is energetically favorable for a dislocation to intersect a void because its core and strain energy is zero within the cavity[5, 21]. A step of length b is created on the entry surface of the void. (iii) The dislocation bows between the voids under increasing ϵ until it is released at the critical resolved shear stress. This always leads to a sharp drop in τ.

The situation is like the orange series in Figure 4.2 for cases where the Shockley partial dislocation separation distance is wide relative to the void size. The partial dislocation closest to the void, the *leading partial*, will in this case be attracted towards the void earlier than the other partial, the *trailing partial*, and the plot of τ will show two distinct drops for the respective attractions. This is indicated by dotted circles in Figure 4.2. The dislocation release process is often also divided into two distinct release/depinning processes corresponding to the two partial dislocations. The critical stress of depinning will be visible as two peaks, indicated in Figure 4.2 by dotted arrows. We normally denote the highest of these two values as being the CRSS for the complete release of the dislocation, but it is also interesting to analyze the behavior of the CRSS for the leading and trailing partial separately.

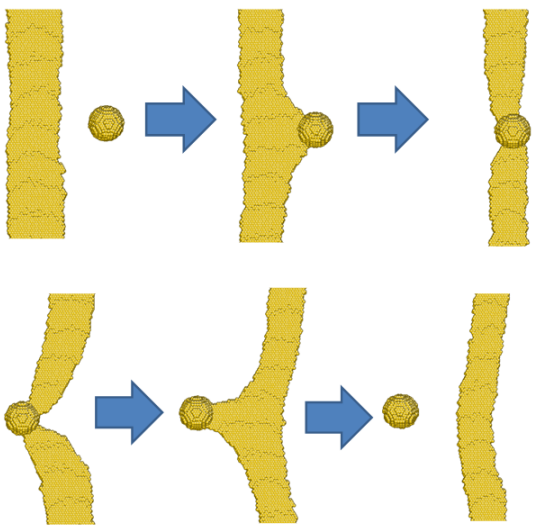

Figure 4.1: Typical dissociated edge dislocation interaction with void. The partials are moving towards the right, colliding with the center of the cavity.The partials are released from the void almost at the same time when critical stress is reached. Atoms that constitute a perfect crystal are omitted, while those that constitute the dislocation, the stacking fault and the void are extracted from the simulation output through common neighbor analysis.

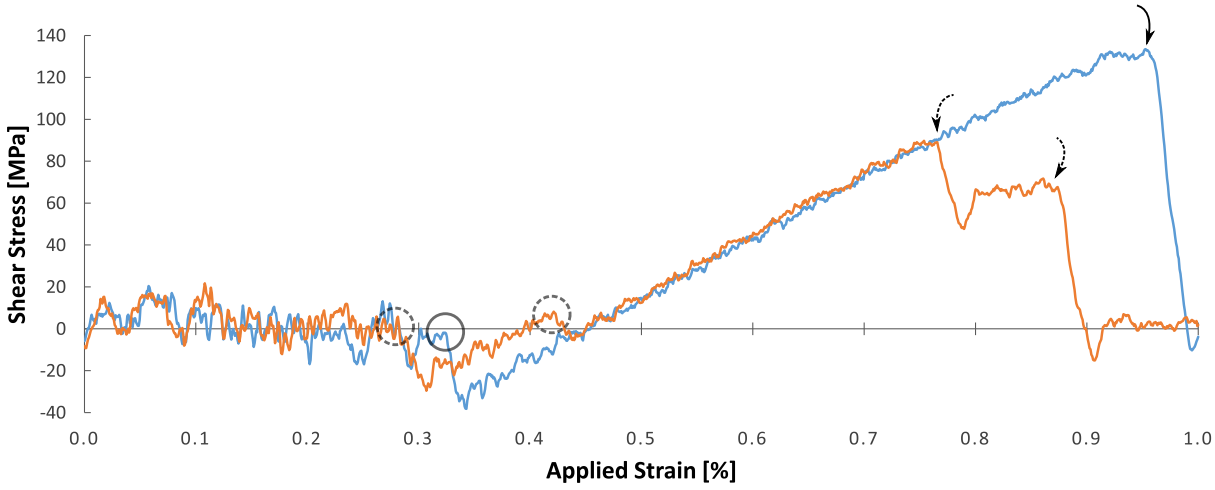

Figure 4.2: Typical simulation output showing shear stress, τ_{xz}, as a function of applied strain for an array of 4 nm diameter voids at $T = 300$ K. The orange series is simulated with an intrinsic stacking fault energy of 14.6 mJ/m^2, the blue with 187 mJ/m^2. The wide stacking fault of the former leads to separate connection to and release from the voids, as indicated by dotted lines.

4.1.2 Shockley Partial Separation Distance

As explained in section 2.2.1, the stacking fault energy of a material affects the equilibrium separation distance between the Shockley partial dislocations. According to Equation2.6, this separation distance is expected to vary proportionally to the inverse of the SFE of the material. A plot of the separation distances expected from Equation 2.6 for the SFE values available to us, those mentioned in Section 3.1.1, is shown in Figure 4.3 as separation distance versus SFE. The Poisson ratio was in this calculation set to 0.33, $a = 3.639$Å, and the shear modulus G was calculated for each potential depending on the elastic constant given for that potential in the appendix, close to ≈ 47 GPa for all potentials.

Simulation results for the same seven potentials are also plotted in Figure 4.3. These values have been calculated by collecting a time average of the separation distance for an edge dislocation in a relaxed simulation cell at the given temperature. The fit between the two series is good, indicating that our simulations replicate the expected stacking fault properties from elasticity theory well. The limited size of the simulation cell might explain the deviation from the expected theoretical value for the lowest SFE potential, as a limited cell size with periodic boundaries might lead to weak repulsive forces between partials across periodic boundaries. This will in effect compress the

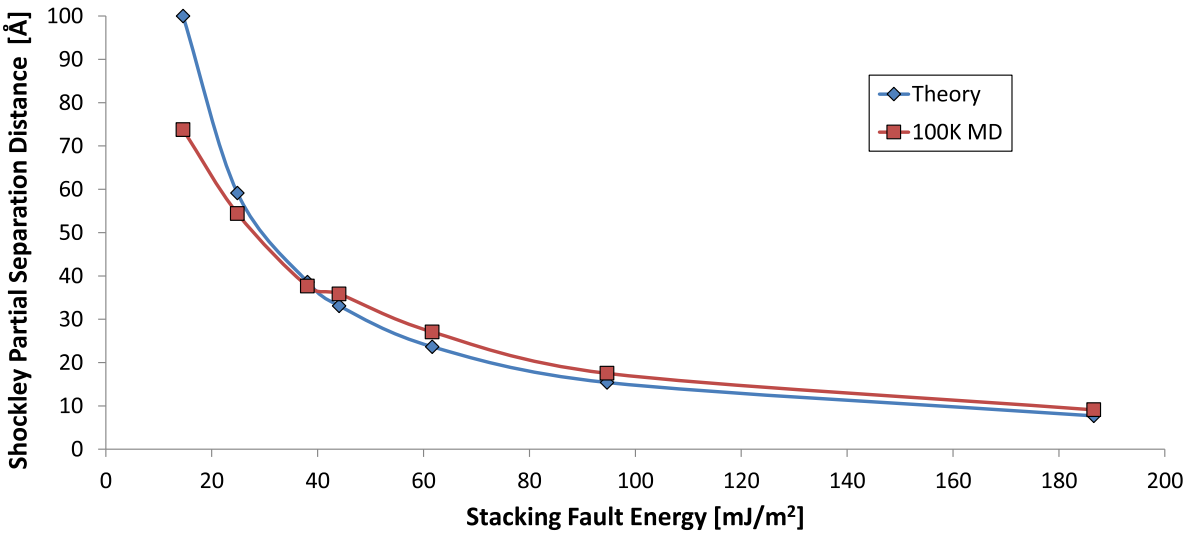

Figure 4.3: Shockley partial dislocation separation distance as a function of SFE. The partials are dissociated from a perfect edge dislocation. Blue line/diamonds show the calculated results of Equation 2.6. Red line/squares show the time averaged separation distance for simulated dislocations at 100K using Mendelev potentials.

width of the stacking fault between the partials.

We note that since the shear modulus G is almost double in value for austenitic stainless steel compared to that for copper, the predicted separation distance will in all cases be almost double of the values given in Figure 4.3.

4.1.3 Effects of Void Size and SFE at 100 K

Let us first focus on the SFE effects found for a single void size. Figure 4.4 shows a plot of CRSS versus SFE for a 2 nm diameter void. The critical stress is presented in units of force per area, Pascal, and represents the critical value of the shear stress σ_{xz} required for the dislocation to overcome the array of voids. This particular void size is chosen for presentation because the partial dislocations are released from the voids both separately and together, depending on the stacking fault energy in the simulated material. It will be shown later that small voids up to 2-3 nm diameter will release the partial dislocations separately as long as the SFE is sufficiently low. Higher values of SFE, or larger voids, retain the leading partial in a pinned state long enough for the trailing partial to also get pinned on the void, leading to a

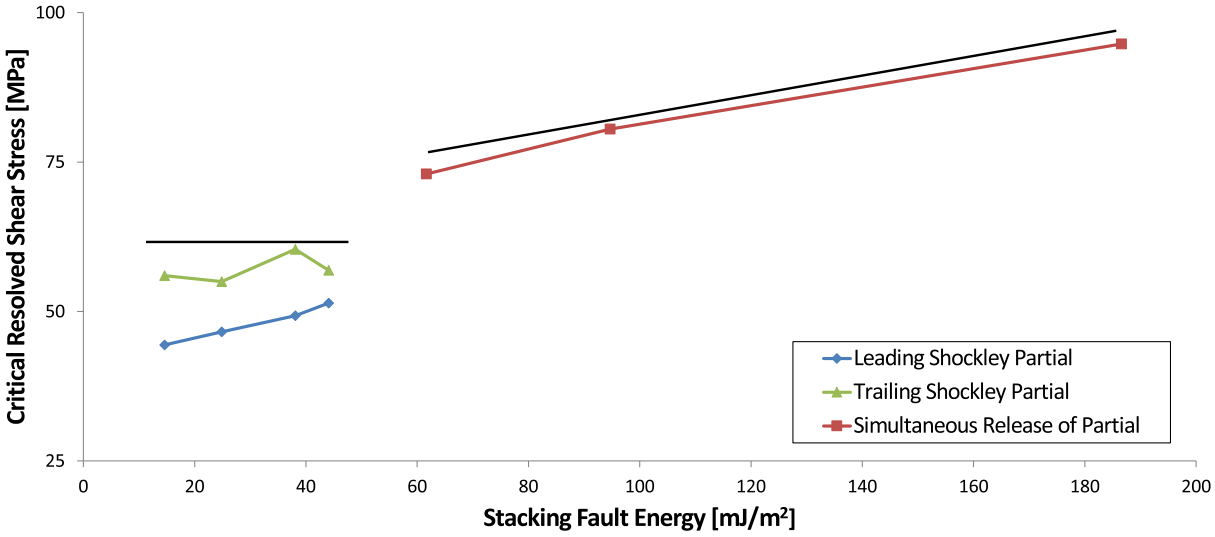

Figure 4.4: Plot of CRSS versus SFE for 2 nm diameter void. Black lines are drawn to visualize CRSS trends. System temperature: 100K.

simultaneous release of the two partials when the required CRSS is reached in the simulation cell.

The dominant critical stress is in this case, Figure 4.4, *independent of SFE* as long as the partials are released separately from the void, that is, for low values of SFE. The critical stress for the leading partial is increasing with increasing SFE, but this is not the case for the dominating trailing partial. The void is in this case considered a "weak" obstacle to dislocation motion. This limited pinning strength leads to an early release of the leading partial. As the stacking fault energy increases to what can be found for regular copper, some 50mJ/m^2, this situation changes. The increased pinning strength of the void will pin the leading partial even as the trailing partial is forced closer to the void, leading to simultaneous pinning of both partials. As the shear stress on the cell increases, both partials will now be released at (almost) the same time. The CRSS dependency on SFE has now changed: the pinning strength of the obstacle is now increasing moderately for increasing SFE. This indicates that the depinning behavior is strongly dependent on the ratio between obstacle strength and SFE.

Let us now look at a complete plot including all simulated void sizes, Figure 4.5. The situation is now more complicated, but we recognize a near-independence of SFE within the area of the figure shaded in red, for low SFE and low CRSS. For very weak obstacles – in this case voids of 1 nm diameter

– the influence of SFE is very weak indeed, and the value of CRSS is in all cases independent of SFE. The effects of varying the SFE in the case of bigger voids are unambiguous however, with higher SFE implying an increase in the pinning strength of the obstacle. The relative impact on CRSS, visualized more clearly in Figure 4.6, is especially visible for intermediate-sized voids: for the $D = 3$ nm sized void the pinning strength (CRSS) for a SFE resembling austenitic stainless steel is $\approx 50\%$ of that found for a SFE typical for copper. The pinning strength for a SFE resembling aluminum is $\approx 150\%$ that of copper SFE. For larger sized voids the impact of the SFE value on the CRSS stabilizes, settling on a$\approx$ 15% difference between copper and steel SFE for the 8 nm diameter void.

As previously mentioned, the Shockley partials are released separately from voids that are relatively weak obstacles and for low values of SFE. The combination of wide stacking faults and small voids enables the two Shockley partials of the dissociated dislocation to overcome the voids separately. The CRSS of the leading partial is dependent on the value of SFE, and behave in a manner similar to the CRSS values obtained in the case of single depinning. The trailing edge behaves differently however: it seems to be largely unaffected by the SFE of the material. This is in contrast to the findings for copper SFE of Hatano and Matsui in [6], where the CRSS of the leading partial is found to dominate the CRSS of the trailing partial for all void sizes. A logarithmic behavior is found by Hatano for the trailing partial CRSS as a function of void size. We are however unable to investigate this claim, as the transition from separate release of the partials to a single process happens for smaller void sizes in our research than in [6]. The simulated cell size is significantly smaller in [6], which as we will see later has a significant impact on e.g. the temperature dependence of the CRSS. This might explain the above mentioned discrepancies.

Figure 4.6 shows a plot of CRSS versus void diameter for five of the seven simulated values of stacking fault energy. Many interesting effects of SFE on the pinning strength of voids are shown here. We have found that the equilibrium separation distance, as displayed in Figure 4.3, between the Shockley partial dislocations can be used as rough indication of the pinning strength dependence on void diameter. For the smallest simulated void with a diameter of 1 nm, the pinning strength is seen to be independent of SFE. As the void diameter increases to 1.4 nm, an elevated value of the CRSS for the highest SFE appears. At this SFE typical of aluminum, the separation distance between partials is ≈ 10 nm. The series with a SFE of 94.7 mJ/m^2 also departs from the lower SFE cases when the void diameter reaches 2 nm, and a clear spread of all results is visible when the void diameter hits 3 nm.

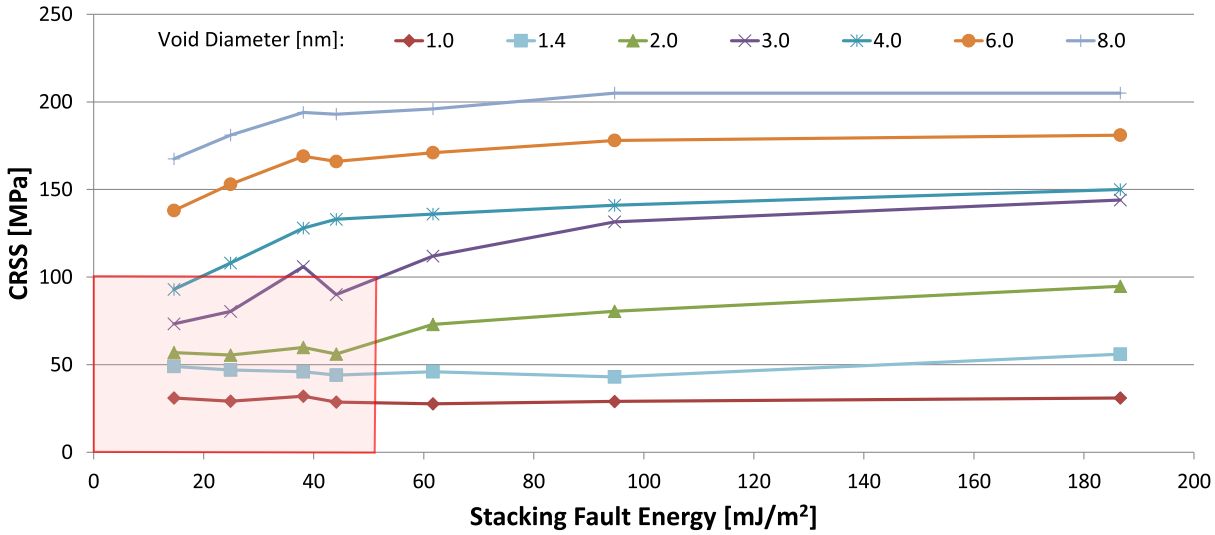

Figure 4.5: Plot of CRSS versus SFE for a variety of void diameters. The area shaded red indicates the approximate region where separate release of partials from the void occurs. System temperature: 100K.

This is consistent with the separation distance of the 38.1 mJ/m^{2}SFE case, as this distance is $\approx$ 35 nm on average. The spread, and therefore the effect of the difference in stacking fault energy between the simulated materials, is at its largest for the 3 nm diameter void. The results for the lowest SFE, typical of austenitic stainless steel, interestingly *never changes slope*. This is also consistent with its equilibrium separation distance, which is in the range 70-90 Å. The spread of the different series is seen to decrease slowly as the void diameter gets closer to 8 nm.

The rough correlation between equilibrium stacking fault width and the temporary change in slope seen in Figure 4.6 is a manifestation of the observed change in critical stress as the depinning process changes from separate to simultaneous release of the two dislocation partials. Figure 4.4 indicates that this change in pinning dynamics is followed by a sudden increase in pinning strength, explaining the behavior recently discussed. It will be shown later that these effects are less systematic for temperatures above 100K.

Continuum theory, as presented in Section 2.2.3, predicts a logarithmic dependence on void size for the CRSS through Equation 2.9. Dissociation of the perfect dislocation is not accounted for in this theory however, which might explain the better theoretical fit for data series obtained with higher-SFE materials. A thorough comparison of simulated CRSS results with the theoretical predictions of Equation 2.9 for edge dislocations in a Cu potential

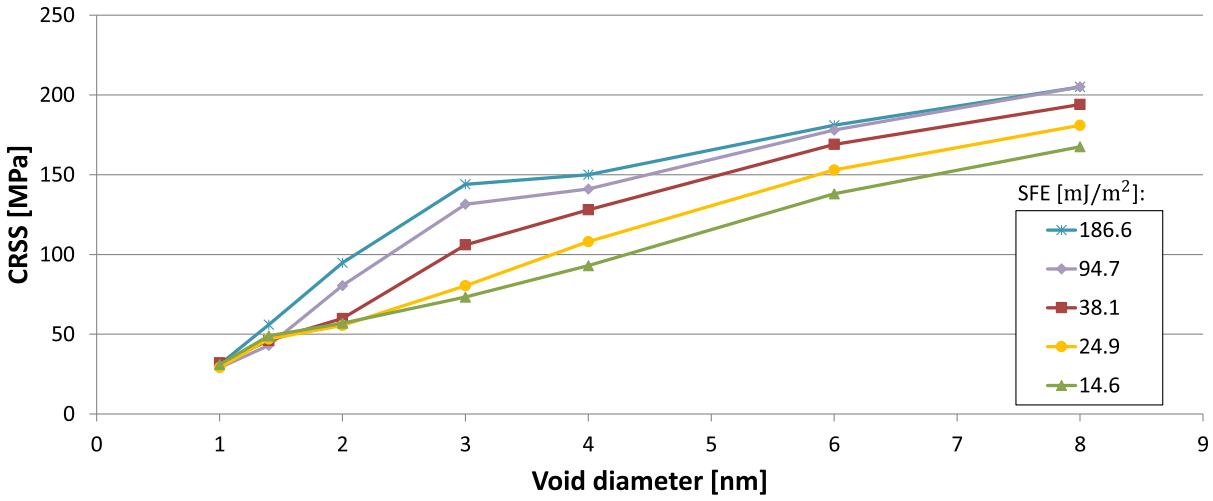

Figure 4.6: Plot of CRSS versus void diameter D for different stacking fault energies. The series marked with green/triangles represents a SFE value typical for austenitic stainless steel, the series in blue/stars resembles typical aluminum SFE and the series in red/squares is close to expected copper SFE. Of primary interest is the vertical spread of the series. System temperature: 100K.

with normal SFE can be found in [5] and [6].

4.1.4 Effects of Impact Parameter and SFE

So far we have limited ourselves to a situation where a dislocation collides with the void center. This is a rather special case, because the relative position of a void to a glide plane is arbitrary. In this section, we change the distance between the void center and the glide plane. We name this distance the "impact parameter", denoted by x/r as a ratio between the distance from the void center and the void radius. (See Figure 3.2.)

Simulation results are displayed in Figure 4.7. The the impact parameter is found to affect the pinning strength in an asymmetric manner. The interaction between the dislocation core and the void is almost negligible when the glide plane of the dislocation falls outside the void surface. This is consistent with the findings of Hatano and Matsui [6], who used a similar MD model of Cu with a different interatomic potential for an edge dislocation and voids in the size range $D = 0.6$ to $D = 5$ nm, with $L = 23$ nm. The asymmetry is expected, as the hydrostatic pressure around the core of an edge dislocation is strongly dependent on the orientation of the dislocation. It is clear from Figure 4.7 that the elastic strain around a dislocation plays an important role in dislocation pinning processes, in addition to the dislocation core. The extra half-plane of atoms that makes up the edge dislocation is seen to interact with the void in such a way that the critical stress is near constant for negative impact parameters. However, as the impact parameter *increases* from zero, the center intersection configuration, we observe that the critical stress falls rapidly. These behaviors show that the strain field, and thereby the hydrostatic pressure, is dominant in the evaluation of critical shear stress.

Figure 4.7 also show that the shape of the distribution of CRSS values as a function of impact parameter is near-independent of SFE. This indicates that the mechanisms controlling the critical stress are not significantly changed as the stacking fault energy changes. One exception however is found in the case of high SFE. As the glide plane of the dislocation falls outside the void surface at negative impact parameters, we observe a generally higher pinning strength than what is found for lower values of SFE. Especially interesting is the high critical stress found in the case of an impact parameter just slightly below -1. Atomistic investigations show that this is caused by *dislocation climb*: As the dislocation core passes in close proximity to the void it is attracted to the void surface, and connects to it through dislocation climb. As climb only occur for high values of SFE, we conclude that climb is only possible when the partial dislocation separation is small.

The large variance in the pinning strength distribution suggests reconsideration of the equal pinning strength assumption in dislocation dynamics

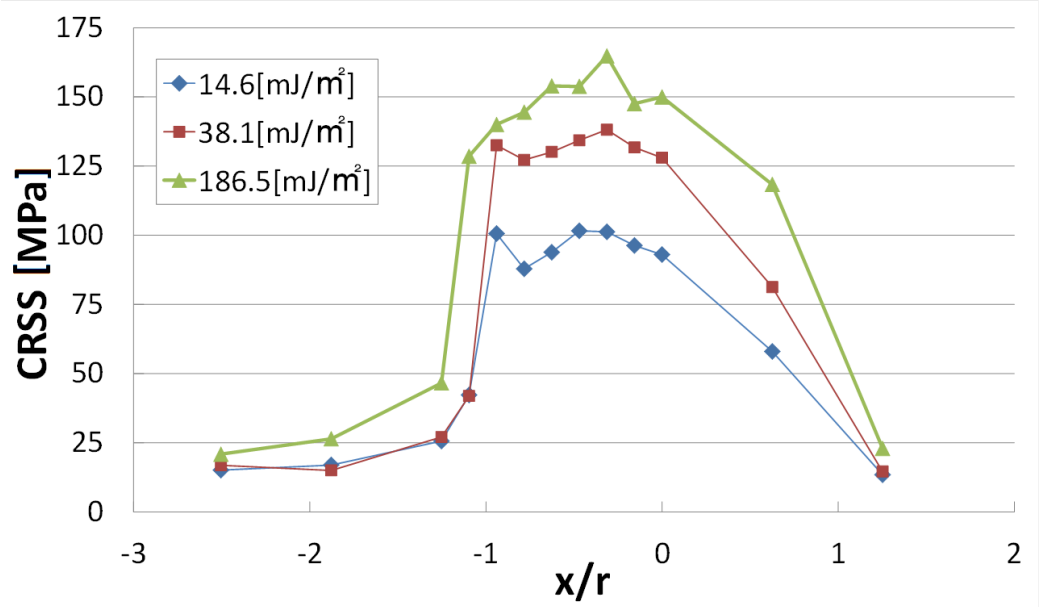

Figure 4.7: Plot of CRSS versus impact parameter. System temperature: 100K.

simulations. Hatano and Matsui suggest a possible correction for normal SFE Cu in [6]. We have shown that this correction should work equally well for materials of lower SFE.

4.1.5 Effects of Elevated Temperature

Hatano and Matsui [6] found no significant variation of τ_c for T in the range 100 to 500 K, a result they attributed to the absence of dislocation climb at release from the voids. The spacing between voids in their simulations were $L = 23$ nm. Osetsky *et al.* [5] used a spacing of 35.5 nm between the voids in their simulations, and observed the same absence of temperature dependence for voids of 2 nm diameter. A significant variation of τ_c on T was however found for 6 nm voids, where the critical stress fell significantly as T increased from 100 to 600 K. Osetsky suggest in [5] that this difference could be explained by the difference in choice of L.

Our results on the variation of τ_c for T in the range 100 to 600 K, with a variety of SFE values are shown in Figure 4.8. The temperature dependence of the CRSS for edge dislocation depinning confirms the findings of Osetsky *et al.*: A significant variation of τ_c on T is only apparent for larger voids. We find almost no temperature dependence for the combinations of SFE

and void size where the partials are released from the voids separately, and only minor decreasing trends with increasing temperature for intermediate sized voids. It is however clear that the effects of increased temperature becomes noticeable for voids of 4 nm diameter and larger. The relative difference in CRSS increases with both increasing void size and increasing material SFE. The SFE dependance is unambiguous: the material with SFE values resembling austenitic stainless steel experiences only one third of the reduction in CRSS brought by the increased temperature. The effect of increasing the temperature from 100 to 600 K is never greater than 7% in the low SFE case, but reaches 25% for high SFE materials. This leads to an interesting effect, displayed in Figure 4.9: For interactions with the largest voids at 600 K the critical stress is effectively the same for both very low and very high values of SFE.

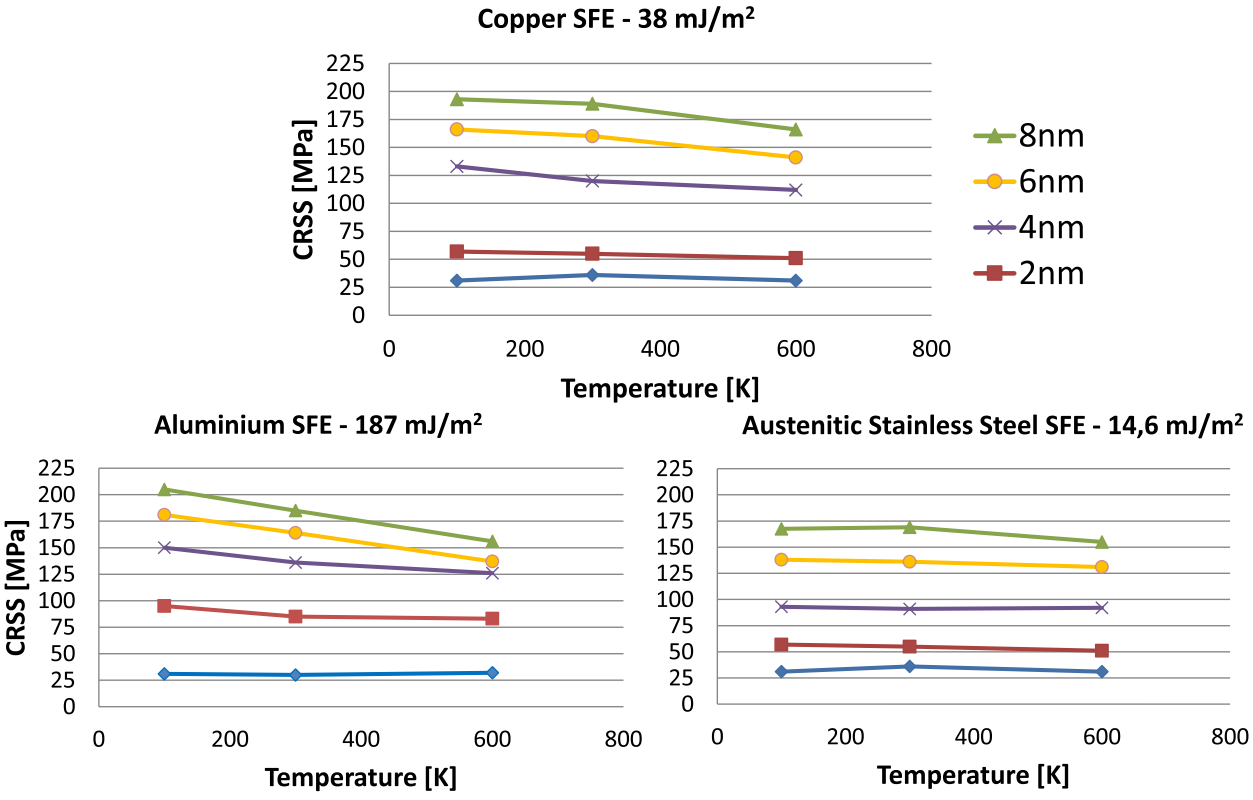

Figure 4.8: CRSS versus temperature [K] three different values of SFE and five different void diameters.

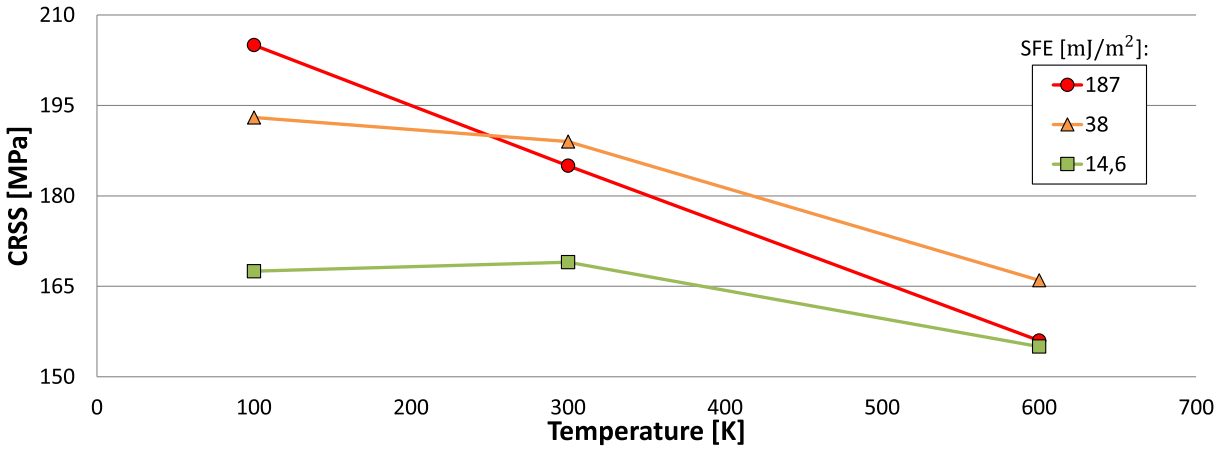

Figure 4.9: Plot of CRSS versus temperature for 8 nm diameter void. The effect of temperature on the CRSS for large voids is higher for higher values of SFE. This makes the CRSS almost independent on SFE for high temperatures. Note the compressed vertical axis.

4.1.6 Effects of Void Separation Distance

The void-center separation distance in all results shown so far have been 35.5 nm. Figure 4.10 display a series of results obtained through a systematic variation of the separation distance L, compared with some theoretical results from dislocation theory. The BKS model as described in Section 2.2.3, Equation 2.9, include the separation distance L both in the multiplication factor and in the logarithm of the harmonic mean between L and void radius r. Figure 4.10 however indicates that our simulation results for Cu (Mishin potential) have a slightly better fit for a modification of Equation 2.9 where L in the harmonic mean has been removed. One possible explanation for this deviation might be that dissociation into Shockley partials is not taken into account in the BKS model. Interestingly we note that the CRSS for both the leading and trailing edge partial dislocations follow the theoretical predictions remarkably well.

Generally, the well-behaved results displayed in Figure 4.18 indicate that our computational model works in a predictable manner even for void separation distances at one third the distance used in our general model. As L is equal to the y axis in our simulation cell due to periodic boundary conditions, we interpret this as a good indication on the stability of the edge dislocation model used in this thesis.

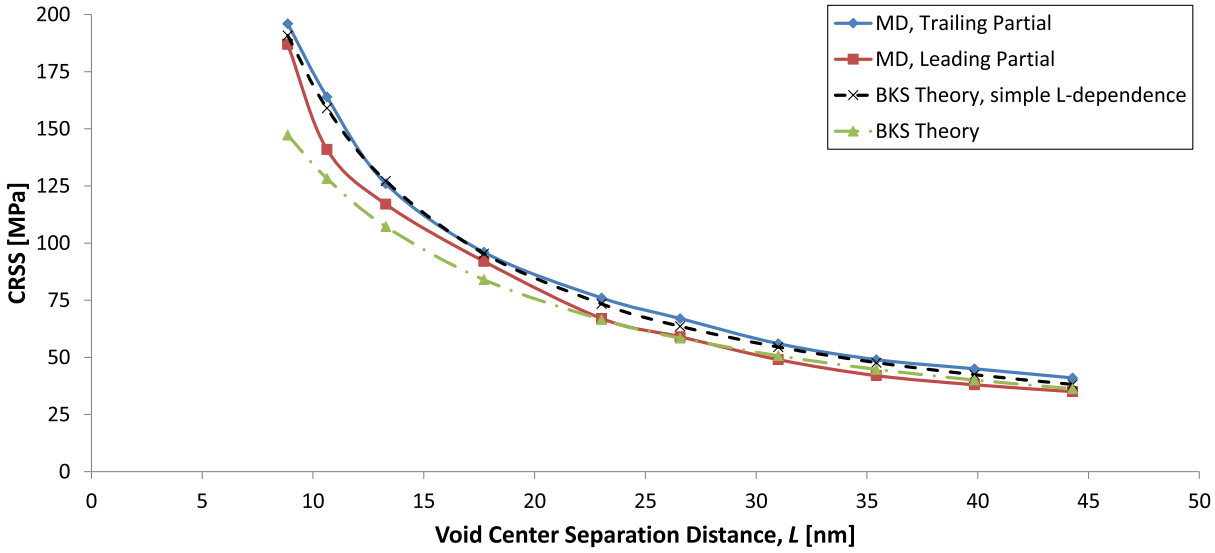

Figure 4.10: CRSS versus void-center separation distance L. Equation 2.9 was used for theoretical calculations. The inclusion of L in the harmonic mean was omitted for theoretical results visualized in black/cross. The adjustable parameter B was set to 0.2. Simulation data is for a void of 2 nm diameter, obtained by use of the Mishin Cu potential. System temperature: 100 K.

4.2 The Screw Dislocation

Complex cross-slip mechanisms make the screw dislocation pinning dynamics *fundamentally different* from the edge dislocation case. We will in the following see varying degrees of cross slip depending on temperature, SFE and void size. The behavior of this cross slip is highly unpredictable. The originally perfect dislocation again dissociates into two Shockley partials in all simulations regardless of interatomic potential, but with an equilibrium separation distance according to the intrinsic stacking fault energy of the potential selected for the simulation.

4.2.1 Description of General Interaction Behavior

The general behavior of the "theoretically predictable" critical stress between dissociated screw dislocations and an array of voids is almost identical to the edge dislocation case, and we will therefore focus only on the added complexities of the screw dislocation interactions in the following. The evolution of shear stress as a function of applied shear strain for screw dislocations is similar to that described in Figure 4.2. As predicted by Equation 2.7 the

equilibrium separation distance between the Shockley partials, and thereby the width of the stacking fault, is however significantly shorter than in the edge dislocation case.

The dissociated Shockley partials of a screw dislocation have edge components and therefore cannot cross-slip. Classical theory therefore requires that for cross-slip to occur, the dissociated dislocation must be constricted, either by the applied stress or by thermal fluctuations, so that the edge components of the partials mutually annihilate. The remaining pure screw dislocation can move freely from the primary glide plane onto another cross-slip plane.

It is clear from all our simulations involving screw dislocations that cross slip always follows constriction on the void surface. Contrary to an edge dislocation, the screw dislocation will not react identically with the two sides of the void. This is due to the directions of the Burgers vectors, as explained in [7]. The most important point is that constriction always occurs at one end of the dislocation, as is evident from Figure 4.11. This asymmetry of constriction on the void surface is explained in terms of the energetics of the Shockley partials. Following Rasmussen *et al.*[4], we refer to the more compressed constriction at the void surface (seen to the left in the red/blue part of Figure 4.11) as *screw-like constriction*, and the less compressed one as *edge-like constriction*. Screw-like constriction is energetically more favorable than edge-like constriction because of the angles formed between the Burgers vectors of the partials and the normal vector of the surface[4].

Cross-slip is clearly visible in Figure 4.11, but it has negligible impact on the CRSS in this specific case. The general behavior is therefore similar to that observed for edge dislocations.

4.2.2 Effects of Void Size, Temperature and SFE

170 separate simulations have been completed in order to investigate the behavior of the CRSS for different stacking fault energies and void sizes. Results obtained with a Mendelev potential with a SFE typical of Cu are shown in Figure 4.12. For the low temperature of 100K, we observe that all simulation results retain a classic predictability. This predictability disappears for all higher temperatures however, as a situation arises where some interactions will behave closely as predicted by continuum theory, while others will experience various forms of complex cross slip - normally with the consequence that the CRSS of the interaction is significantly increased.

From figure 4.12 we see that the critical stress in overcoming the void is increasing with increasing void size. This is consistent with our expectations,

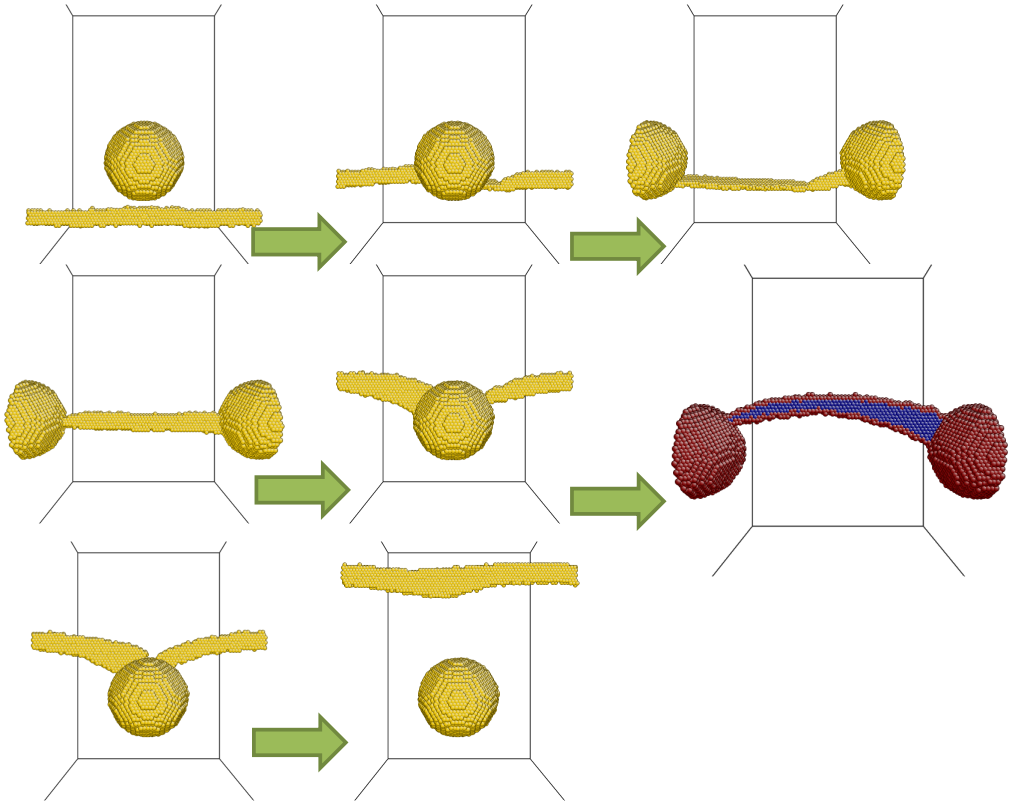

Figure 4.11: An example interaction between a 6 nm diameter void and a dissociated screw dislocation. The method of visualization is the same as in Figure 4.1. The dislocation is moving upwards as a result of applied shear strain on the simulation cell. The cross slip is seen to start on the right side of the void, and the constriction, as seen in the red/blue part, is clearly not symmetric with respect to right and left.

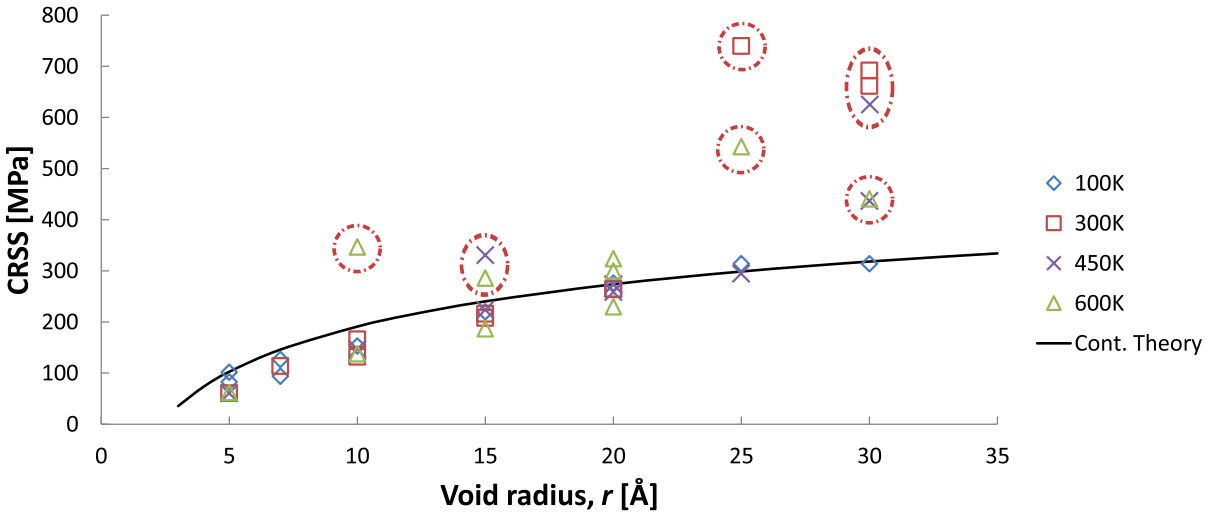

Figure 4.12: Plot of CRSS versus void radius r for screw dislocation interactions. The potential used was a Mendelev potential with a SFE of 38 mJ/m^2. The solid line is Equation 2.9 with $B = 0.7$.

and resemble the behavior seen for edge dislocation interactions. Continuum theory predicts a logarithmic relationship between critical stress and void size, as expressed through Equation 2.9. It is challenging to decide whether we can confirm the theoretical expectation, but the data does however seem to fit remarkably well to the 100 K results for the value of B chosen. For comparison, Osetsky *et al.* use $B = 1.52$ in their comparison of theory and edge dislocation results in [5], but for systems at zero kelvin. It is clear that the BKS equation is more accurate for screw dislocations than for edge dislocations as long as we ignore the unpredictable higher temperature part of the results. This could however be expected, as the dissociation separation is shorter for screw dislocations: dissociation is not accounted for in Equation 2.9. The continuum theory discussed in this report is also only developed for quantitative considerations at low temperatures.

As the temperature reaches 300 K in Figure 4.12 the behavior becomes unpredictable for void sizes bigger than 4 nm diameter. The CRSS is in these cases strongly elevated at over twice the expected value. Inspection of the atomistic time evolution shows that constriction of the dislocation at the screw-like void surface interface initiates a cross slip to a perpendicular (111) glide plane, an example of this is visible in Figure 4.13.

For 300 K and 5/6 nm diameter voids we sometimes get a situation where this cross slip spreads to the entire width of the dislocation, with the result that the dislocation is almost released from the voids in a direction perpen-

dicular to the original glide plane. This requires a complete cross slip of the entire dislocation, and therefore also require constriction at the edge-like void surface. As shown by Rasmussen *et al.* in [4], the energy required for such a constriction is relatively high, high enough that this only happens in approximately one out of three of our simulations at 300 K. In these cases the dislocation quickly escapes to the z surface of the simulation cell, resulting in values of CRSS not relevant to this study. More often however, the dislocation bows out strongly on the perpendicular glide plane but eventually cross slips to a glide plane parallel to the original glide plane. It is now released from the voids in the expected direction with a jog or superjog connecting the two parts of the dissociated dislocation. The shear stress experienced by the dislocation on a glide plane perpendicular to the original glide plane is calculated to be approximately one third of the main xz shear stress.

The situation described in the previous paragraph also occurs for simulations at 450 K, but not at 600 K. For both of these temperatures however, a new characteristic interaction appear. Complex double cross slip in these cases sometimes lead to small immobile loops being formed at the location of jogs between different glide planes. These immobile structures take on different forms, and lead to different and unpredictable pinning characteristics. Examples of these structures are seen in figure 4.13. This happens for all voids larger than 2nm diameter, and results in a 30-100% increase in CRSS. This increase in critical stress is attributed to the fact that immobile structures effectively decreases the apparent separation distance between voids, completely impeding dislocation motion in affected locations.

Simulation results for CRSS versus void size for a material potential with a SFE of 14.6 mJ/m^2 are displayed in Figure 4.14. The tendencies are similar to those found in the simulated material with a SFE of 38 mJ/m^2, but there are several striking differences. If we ignore the special cases circled in red, CRSS is still increasing monotonously with increasing void size. However, all values are 5-30% lower than for "normal copper" SFE, and the results show a more apparent linear behavior than previously. The fit with Equation 2.9 for the chosen value of B is still quite good however. The value of B has to be lower in order to fit the results for this value of SFE than it had to be for SFE typical of Cu, as B is the only parameter that can change in the BKS equation.

Interactions deviating strongly from continuum theory predictions are now *only found for the highest simulated temperature,* 600 K. The increased separation distance between the Shockley partials originating in the lower SFE makes dislocation constriction at the void surface more difficult, and increases both the stability and predictability of the dislocation - void inter-

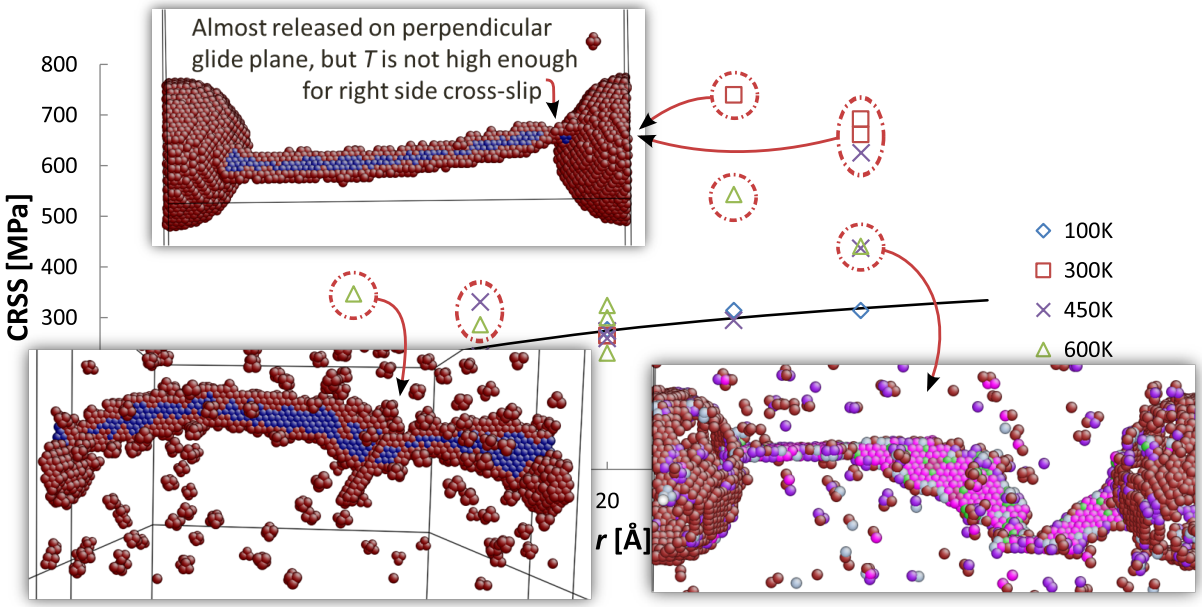

Figure 4.13: Examples of critical atomistic configuration for 38 mJ/m^2 SFE simulations. The noise in the figures is due to thermal vibrations: the common neighbor analysis fails to ignore atoms temporarily out of normal lattice configuration due to high thermal activity. This can be corrected by the use of thermal averaging in the output data. Figure 4.12 is in the background.

actions. Both the stability and predictability break down at 600K however, resulting in strongly elevated values of CRSS circled in red in Figure 4.14.

Examples of critical atomistic configurations are displayed in Figure 4.15. Dislocation constriction at the screw-like void surface leads to multiple cross-slip that spreads across the width of the dislocation. The elevated CRSS values are sometimes caused by large cross-slipped segments that are immobile in the original glide plane direction, and sometimes by immobile loops created at the location of jogs between dislocation parts found in the original glide plane and a parallel plane due to double cross-slip. It is important to note that even though cross-slip occurs in all simulations at 600 K, there is only a certain probability that this will lead to CRSS values above those expected. This is clear from the results, where many simulations conducted at 600 K result in CRSS values slightly smaller than those expected and obtained at other temperatures. No unpredictable values of CRSS are found for voids smaller than 3 nm diameter.

Simulation results presenting CRSS versus void size for a material poten-

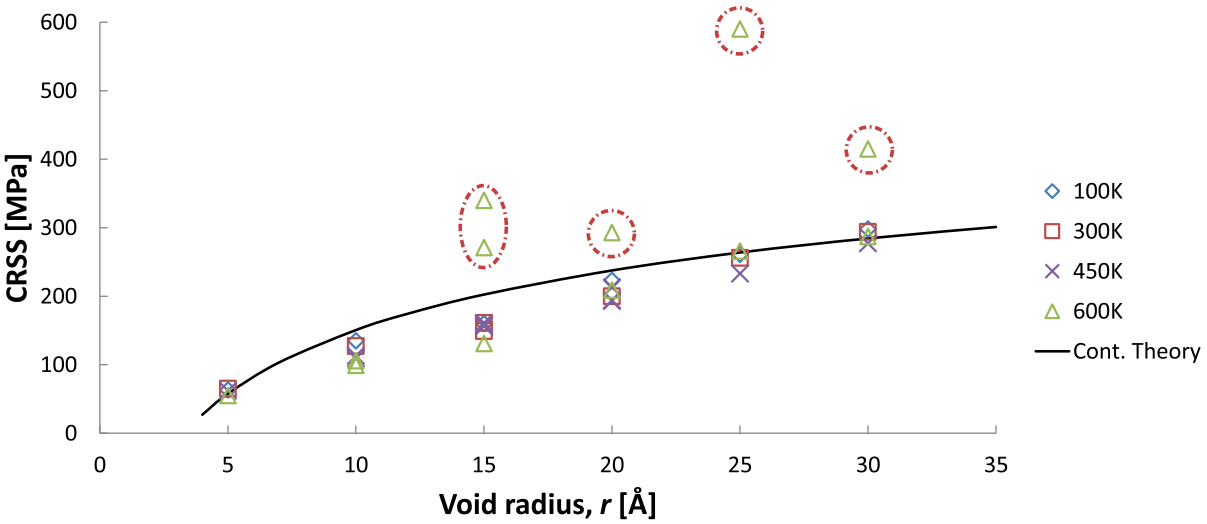

Figure 4.14: Plot of CRSS versus void radius r for screw dislocation interactions. The potential used was a Mendelev potential with a SFE of 14.6 mJ/m^2. The solid line is Equation 2.9 with $B = 0.45$.

tial with a SFE of 187 mJ/m^2 are displayed in Figure 4.16. The tendencies are similar to those found in the simulated material with a SFE of 38 mJ/m^2, but there are again several striking differences. If we ignore the special cases circled in red, CRSS is still increasing monotonously with increasing void size. However, all values are now 5-30% higher than for "normal copper" SFE, and the results might indicate a closer logarithmic fit.

Inspection of the atomistic time evolution for the results involving this higher SFE show that cross slip is now happening at a very high rate. The separation distance between the Shockley partials is now very small - in fact the partial dislocations are barely separated at all. This makes screw-like constriction at the void surface very probable, even for low temperatures, and indeed we find that this is the case in our simulations. This frequent cross-slip only leads to unpredictably high values of CRSS in some cases however, as a high rate of cross-slip also means that the dislocation easily cross-slips back to a glide plane parallel with the original one if it gets stuck in a perpendicular glide plane. At 100 K we find that the CRSS normally shows the predicted behavior. Simulations have shown one striking deviation, circled in the top left of Figure 4.16. This result might indicate that immobile structures created at low temperatures, however improbable, are extraordinarily strong obstacles to dislocation movement.

All other cases of elevated CRSS occur at either 300 or 450 K, but values

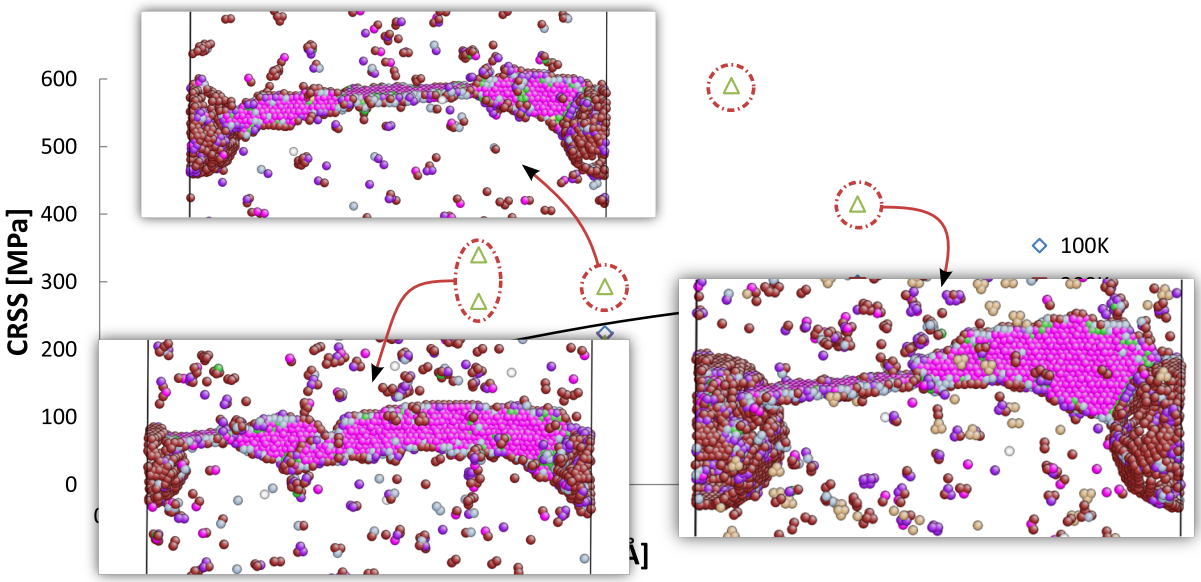

Figure 4.15: Examples of critical atomistic configurations for 14.6 mJ/m^2 SFE simulations. Figure 4.14 is in the background.

of CRSS within the expected range are also found at these temperatures. Enhanced pinning is only found for voids of 2 nm diameter or larger. Remarkably, results for 600 K simulated conditions show no sign of significantly enhanced pinning.

Examples of critical atomistic configurations are displayed in Figure 4.17. It is clear from inspection of all cases of enhanced pinning that the elevated values of CRSS are due to multiple cross-slip creating immobile obstacles. These obstacles are, as usual, always created at a jog between two dislocation parts in different parallel glide planes.

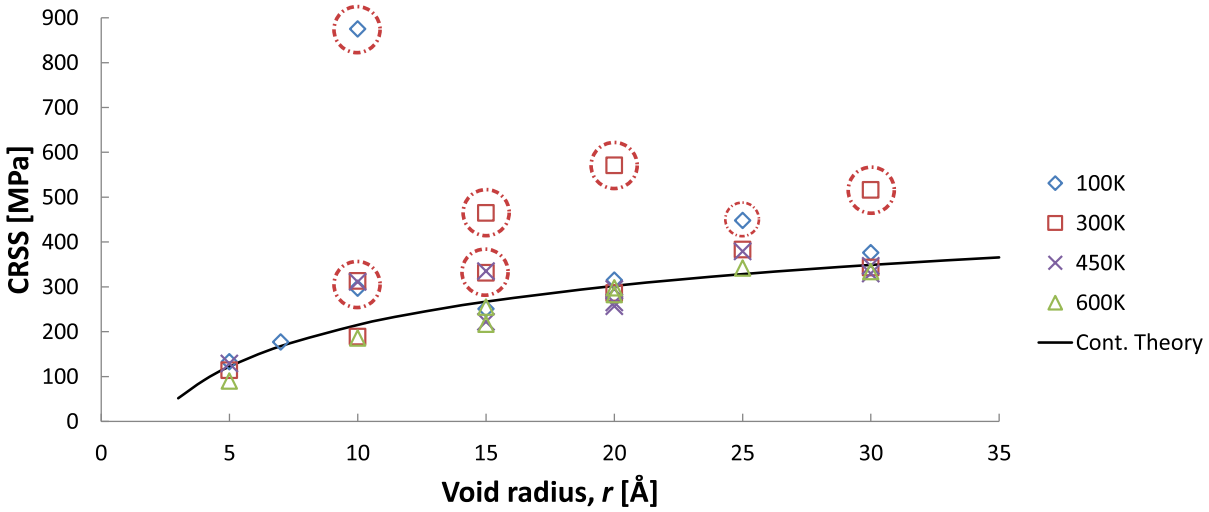

Figure 4.16: Plot of CRSS versus void radius r for screw dislocation interactions. The potential used was a Mendelev potential with a SFE of 187 mJ/m^2. The solid line is Equation 2.9 with $B = 0.9$.

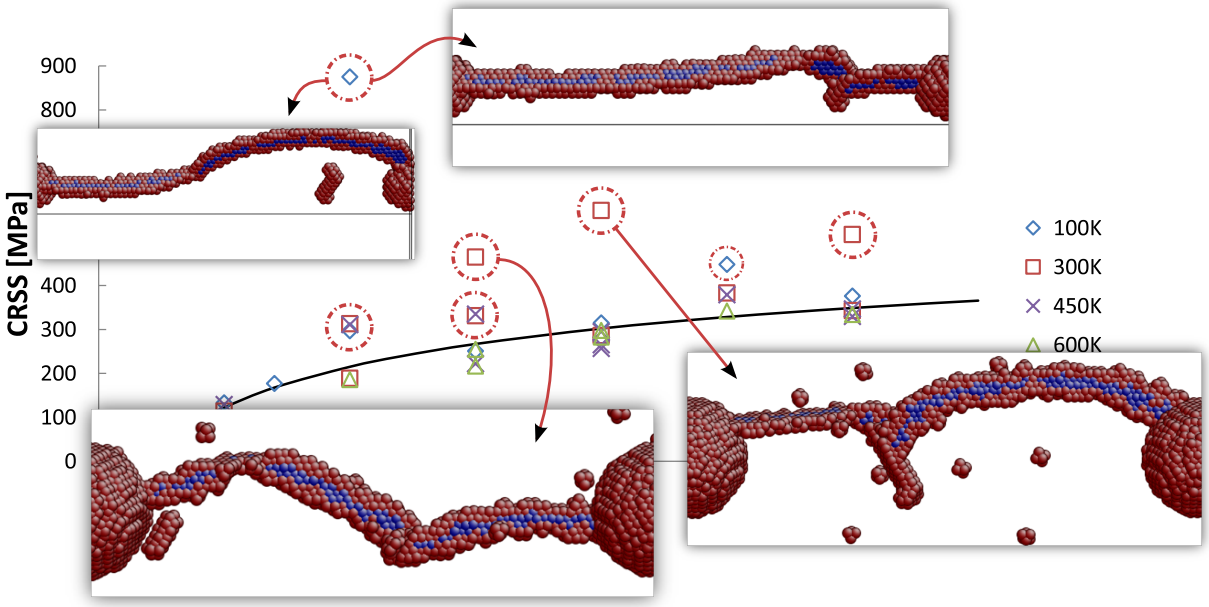

Figure 4.17: Examples of critical atomistic configuration for 187 mJ/m^2 SFE simulations. Figure 4.16 is in the background.

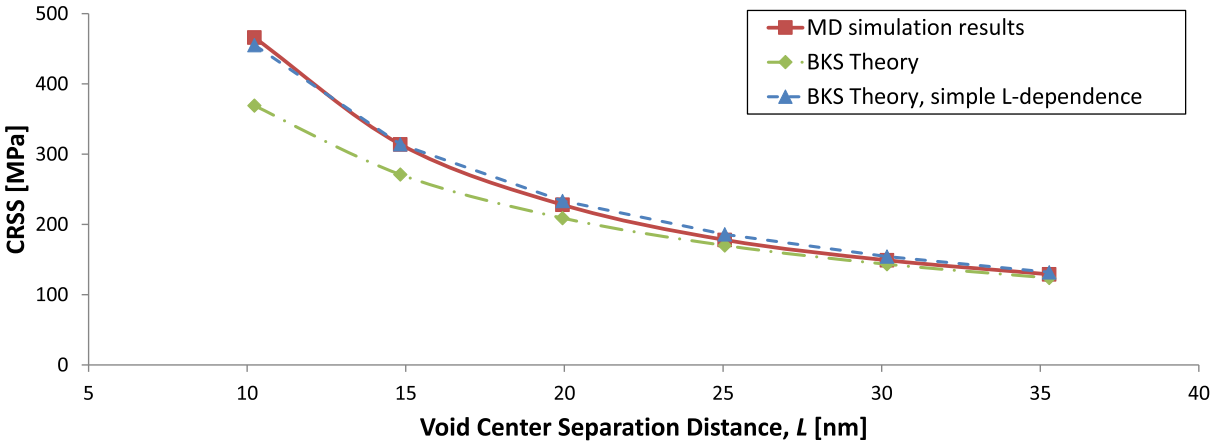

Figure 4.18: CRSS versus void-center separation distance L. Equation 2.9 was used for theoretical calculations. The inclusion of L in the harmonic mean was omitted for theoretical results visualized by triangles. The adjustable parameter B was set to 0.35. Simulation data is for a void of 4 nm diameter, obtained by use of the Mishin Cu potential. System temperature: 100 K.

4.2.3 Effects of Void Separation Distance

The void-center separation distance in all results shown so far have been 20 nm. Figure 4.18 display a series of results obtained through a systematic variation of the separation distance L, compared with some theoretical results from dislocation theory. Just as in Section 4.1.6 for the edge dislocations, we again conclude from Figure 4.18 that our simulation results for Cu (Mishin potential) have a better fit for a modification of Equation 2.9 where L in the harmonic mean has been removed. One possible explanation for this deviation might be that dissociation into Shockley partials is not taken into account in the BKS model. Interestingly, this appears to be the case even though the void simulated in Figure 4.18 is such a strong obstacle that the release from the void is simultaneous for the two partials.

Generally, the well-behaved results displayed in Figure 4.18 indicate that our computational model works in a predictable manner even for void separation distances at half the distance used in our general model. As L is equal to the x-axis in our simulation cell due to periodic boundary conditions, we interpret this as a good indication on the stability of the screw dislocation model used in this thesis.

4.3 Further Discussion

As explained by Domain and Monnet [28], the time available for thermal activation to occur in MD simulation is short. The activation energy is therefore small and interpretation of stress-dependencies in terms of mechanisms is problematic. We have in our research conducted some investigations into the impact of the choice of strain rate ϵ, and we were able to show that a change in strain rate by a factor of five did not significantly alter our simulation results. As a lower strain rate increases the computation time needed to obtain a given strain in the simulation cell however, we were not able to verify the stability of our results for stain rates lower than 1×10^6 s^{-1}. It is easier to obtain higher activation energies through the use of elevated temperatures, and in this regard we can assume that MD results conducted at high system temperatures resemble reality to a better extent.

We chose simulation cell dimensions similar to those chosen by Osetsky in [5] for edge dislocation simulations, and similar to the dimensions chosen by Hatano in [7] for screw dislocations. Hatano also investigated edge dislocation interactions in [6] with the smaller cell size used in [7]. We concluded in Section 4.1.4 that the temperature dependence for Cu SFE on CRSS found by us for edge dislocations resemble the dependence found by Osetsky. This temperature behavior was, as previously mentioned, not found by Hatano in their simulations with the smaller cell size for the edge dislocation. This might indicate that our results for the screw dislocation, conducted with the smaller Hatano cell size, could change behavior if conducted with the larger cell size used for edge dislocations.

Pinning dynamics between arrays of voids and screw dislocations has previously been investigated by Hatano *et al.* in their paper "Void-induced cross slip of screw dislocations in fcc copper" (2008)[7]. In general, the conditions for their simulations are similar to those in this report. However, there are some differences: They utilized a many-body interatomic potential by Finnis and Sinclair [29], with parameters optimized for copper [30]. This results in a stacking fault energy of 36 mJ/m^2in their simulations. The loading of the simulation cell in shear is done by moving the free surfaces of the cell anti-parallel to each other at constant speed, in contrast to our dispersed displacement. The shear stress, as used in the measure of CRSS, is measured on one of the two surfaces: the total force acting on the surface atoms divided by the area. In contrast, we gather shear stress information from the entire simulation cell.

The findings of Hatano are similar to what is reported in this report for a copper potential of normal SFE. Continuum theory and the BKS equation is found to predict CRSS values well, up to 300 K. Elevated values of critical

stress is found for voids of 4 and 6 nm diameter at 300 K, and it is concluded that this critical stress is not uniquely determined by the configuration of the system. It is also concluded in [7] that there always will be a significant increase in critical stress for large voids at 300 K, and for all void sizes at higher temperatures. This is in conflict with the results presented in Figure 4.12, where deviations from the theoretical expected critical stress is shown to occur with only a finite probability for all temperatures above 300 K. Significantly elevated CRSS is found mostly for voids of 5 or 6 nm diameter, and we fail to replicate the consistent increase in critical stress found for 450 K in the paper by Hatano. The explanations of these differences are assumed to lie within one or several of the differences in simulation procedure and simulation conditions recently mentioned.

It is concluded in [7]that cross slip on the void surface is a thermally activated process because no partial cross slip is observed from 0 to 150 K. We have however observed partial cross slip at 100 K for stacking fault energies ranging from copper values ($\approx$ 40 mJ/m^2) to aluminum values ($\approx$ 190 mJ/m^2). In most cases this cross slip is only temporary, and does not significantly contribute to the CRSS of the affected interaction processes. For high SFE however, the creation of an immobile structure has been observed as displayed at 100 K in Figure 4.16. This indicates that whereas the probability for cross slip with consequences is very low at low temperatures, it can happen. The CRSS value of this simulation result is the highest of all results, indicating that the immobile structure is a very strong obstacle at low temperatures where thermal activation is less frequent.

A big part of the focus in this report is on the difference in interaction processes between stacking fault energies typical of copper and austenitic stainless steel. We have, where possible, tried to quantify these differences, and it is therefore important to mention one more time that the shear modulus G of actual austenitic stainless steel is approximately twice the value of G in copper. As G is a multiplicative factor in Equations 2.6, 2.7 and 2.9, it is reasonable to assume that any implication and effect of differences in SFE found in this report will be even more significant for actual stainless steel.

Some limitations and challenges have been discussed as the results were presented. Of major concern for collections of MD simulations is the uncertainty that follows the very limited sample size of results for similar interactions. This is a consequence of the heavy computing power requirements that arise for simulations of several million atoms. More definite and accurate conclusions would have been possible if more concluded simulations were available, but we have tried to run extra near-identical simulations for interactions were the results displayed significant fluctuations. This was done in order

to gain control of the uncertainties involved in the presented material. The reduced cell size chosen for the screw dislocation made it possible to study a greater number of interactions, which is important because of the unpredictable behavior found in the pinning of screw dislocations. It would however be interesting to compare our results with results from bigger cell size simulations.

Chapter 5

Conclusion

Molecular Dynamics simulations have been conducted in order to highlight the implications of stacking fault energy on the interaction between dissociated dislocations and voids. A recently developed set of interatomic potentials with a range of stacking fault energies based on FCC copper was used in order to investigate the critical resolved shear stress and other details for a range of void sizes, temperatures, impact parameters and void separation distances.

The value of SFE in the simulated material was found to have implications for all varieties of dislocation - void interactions. Previous work on the subject conducted by Osetsky *et al.* [5, 10, 24] and Hatano *et al.*[6, 7] was used as a basis for the investigations, but was extended with new information on the influence of stacking fault energy. Their results and conclusions have been discussed throughout the thesis work, and while most results are pointing in the same direction some discrepancies have been discovered.

Changes in SFE are found to affect the pinning interactions between dissociated edge dislocations and voids in a relatively weak but systematic manner. This is also the case for dissociated screw dislocations, but with an added layer of complexity: SFE was also shown to have a major impact on the predictability and temperature dependence of the interactions between voids and screw dislocations.

5.1 Edge dislocation – void interactions

- For edge dislocations the influence of SFE was shown to be negligible for voids of diameter smaller than 2 nm, as the trailing partials dominate the overall CRSS at these void sizes. A SFE dependance was found for the leading partials in these cases.

- For larger voids up to 8 nm diameter a SFE resembling typical SFE values typical of austenitic stainless steel (14.6 mJ/m^2) displayed a reduction in CRSS on the order of 15 - 30 % compared to typical copper (38 mJ/m^2) at 100K.

- Temperature effects were studied up to 600K, showing that whereas increased temperature generally lowers the CRSS, it is only significant for larger voids and for high values of SFE. This interestingly implies that the expected CRSS for large voids (8 nm diameter) at 600 K is the same for the entire range of SFE values (14.6 to 187 mJ/m^2).

- The results are seen not to fit very well with continuum theory, most probably due to the dissociated nature of dislocations in FCC metal. This is also consistent with the observation that theoretical predictions fit better for large voids and high values of SFE.

- Stacking fault energy is found to have only a minor impact on the distribution of CRSS as a function of impact parameter. This indicates that corrections done in order to compensate for the randomness of impact parameters in real metals can be valid also for materials of lower SFE.

- Indications of climb motion was found, even if it is not expected in low SFE FCC metal, for very special conditions of impact parameter and SFE.

5.2 Screw dislocation interactions

- Complex cross-slip mechanisms made the screw pinning dynamics *fundamentally different* from the edge dislocation case.
- Relative to typical copper, SFE resembling that of austenitic stainless steel generally reduces the CRSS for void pinning with 5 – 30 %, if we ignore elevated results resulting from cross-slip.
- The cross slip is initiated by asymmetric constriction on the void surface. Temperature affects the impact and dynamics of this constriction. Cross slip may lead to *highly unpredictable* void pinning dynamics, mainly through multiple cross slip and its consequences by the creation of immobile dislocation structures.
- The value of SFE is shown to be very influential on the distribution, probability and form of complex cross slip mechanisms, which may double or triple the pinning strength of voids.
  - For low austenitic stainless steel SFE, CRSS values elevated above the expected due to cross-slip is only found at 600 K. This is in strong contrast to the results for intermediate and high SFE.
  - The probability of cross-slip induced non-predictable CRSS values change depending on void size, temperature and SFE, but range from 20 - 100 % in the available results.
- CRSS generally follows a logarithmic dependence on void size, as predicted by continuum theory. The fit is however of different quality for different values of SFE, and fit can only be assured by modification of the empirical parameter in the BKS theory.

5.3 Further Work

The effort of evolving elasticity theory through scientific computing has only just begun. The interaction mechanisms between dissociated dislocations and voids are complicated in nature, and will require a lot of multiscale computing effort before the interaction processes are mapped out to a predictable degree. Progress is rapid however, and as interatomic potentials are evolving in a pace similar to that of ever faster computers, we will surely see many interesting contributions to dislocation theory in the near future. Below are some specific suggestions on how the work conducted in this specific thesis work could be expanded and improved upon:

- Reduce CRSS uncertainty by running more simulations. Randomness of simulations can be improved by small changes in cell size and other parameters, as this may prevent resonance effects and similar. Using a different velocity distribution for the temperature generation has been found to not always be enough, as many systematic errors may stay hidden.
- MD simulations simulate interactions at extreme strain rates. The influence of these high strain rates on both screw and edge simulations should be investigated in further detail.
- The comparison of simulated results with continuum theory should be solidified. Differences between different theoretical models should be investigated further.
- Continue work on classification of complex CRSS results for the screw case. Atomistic inspection on the exact nature of the immobile structures created by cross-slip turned out to be very challenging.
- Investigate screw dislocation interactions with larger cell-sizes in order to better classify cross slip behavior. More simulations are needed in order to make more accurate predictions on the probability of elevated critical stress as a function of void size, SFE and temperature.
- Expand the investigation of both edge and screw dislocation interactions to more complicated cases. Interactions for a more random placement of voids could be a start, but poses challenges to the periodic boundary conditions and the PAD model.
- Results should be classified in a systematic manner so that theoretical prediction models can be improved.

Chapter 6

Appendix

6.1 Detailed information on the utilized interatomic potentials

Table 6.1 presents all known information regarding the interatomic potentials used in this thesis. The seven Mendelev potentials used are here represented by their version number, but they have been referenced in the main text by their intrinsic stacking fault energy in [mJ/m^2].

Property	Target value	Mishin EAM1	v. 5.7	v. 5.16	v. 6.1	v. 6.2	v. 6.3	v. 6.4	v. 6.5
a (fcc) (Å)	3.640	3.615	3.639	3.639	3.639	3.639	3.639	3.639	3.638
E_{coh} (fcc) (eV/atom)	-3.540	-3.540	-3.283	-3.423	-3.416	-3.425	-3.429	-3.428	-3.427
E_f^v (unrelaxed fcc) (eV/atom)	1.074	1.309	1.065	1.127	1.140	1.132	1.114	1.086	1.031
E_f^v (relaxed fcc) (eV/atom)		1.274	1.050	1.107	1.118	1.108	1.097	1.073	1.025
E_f^m (fcc) (eV/atom)		0.689	0.988	0.917	0.907	0.905	0.926	0.948	0.995
E_D (fcc) (eV/atom)	2.05	1.963	2.038	2.024	2.025	2.013	2.023	2.021	2.019
C_{11} (GPa)	170	170	175	174	174	173	175	175	178
C_{12} (GPa)	123	123	128	127	127	128	127	127	125
C_{44} (GPa)	76	76	84	84	84	84	84	84	83
E_f^i (<100> fcc) (eV/atom)	2.93	3.08	2.81	2.81	2.81	2.82	2.82	2.82	2.81
d^i (<100> fcc) (Å)	2.162	2.168	1.992	2.074	2.074	2.076	2.074	2.074	2.074
(<100> fcc) (meV/Å^2)		84.0	67.6	74.8	77.7	78.9	72.1	66.1	52.6
(<110> fcc) (meV/Å^2)		92.1	72.0	79.7	82.2	83.2	77.4	72.0	60.2
(<111> fcc) (meV/Å^2)		77.4	56.3	63.7	66.7	67.8	61.0	54.6	41.0
Intrinsic stacking fault energy (meV/Å^2)	2.81	2.77[§]	2.377	2.75	1.551	0.910	3.847	5.907	11.641
Extrinsic stacking fault energy (meV/Å^2)			2.379	2.76	1.551	0.910	3.845	5.910	11.649
Twin boundary energy (meV/Å^2)	1.50	1.386[§]	1.189	1.377	0.776	0.455	1.923	2.955	5.824
a (bcc) (A)	2.894	2.868	2.895	2.894	2.894	2.894	2.894	2.893	2.893
$E_{fcc\ bcc}$ (eV/atom)	0.035	0.046	0.040	0.041	0.041	0.040	0.042	0.043	0.046
a (hcp) (A)	2.561	2.556	2.569	2.568	2.569	2.569	2.568	2.567	2.564
c (hcp) (A)	4.232	4.162	4.211	4.211	4.210	4.209	4.212	4.215	4.224
$E_{fcc\ hcp}$ (eV/atom)	0.007	0.008	0.007	0.008	0.0044	0.0026	0.0109	0.0168	0.0331
R_F (eV/Å)	0.000	0.123	0.492						
d_{liquid} (T=1356 K) (atom/Å^3)	0.0761	0.0745	0.0762	0.0763				0.762	0.761
T_{melt} (fcc, K)	1356	1326	1353	1353	1352	1349	1355	1356	1351
H_{melt} (fcc, T=1356 K) (eV/atom)	0.1347	0.125	0.142	0.130	0.130	0.130	0.129	0.129	0.127
V_{melt} (fcc, T=1356 K) (%)	4.25	5.00	3.63	3.44	3.44	3.53	3.44	3.54	3.53

Table 6.1: Data for the interatomic potentials used in this thesis. Provided by Mikhail Mendelev, Ames Laboratory, U.S. §: These values were not checked by Mendelev, but were taken from [27].

Bibliography

[1] S. Maloy, M. James, G. Willcutt, W. Sommer, M. Sokolov, L. Snead, M. Hamilton, and F. Garner, "The mechanical properties of 316L/304L stainless steels, Alloy 718 and Mod 9Cr-1Mo after irradiation in a spallation environment," *Journal of Nuclear Materials*, vol. 296, no. 1-3, pp. 119–128, 2001.

[2] D. Hull and D. J. Bacon, *Introduction to Dislocations*, 4th ed. Butterworth-Heinemann, 2001.

[3] G. Lucas, "The evolution of mechanical property change in irradiated austenitic stainless steels," *Journal of nuclear materials*, vol. 206, pp. 287–305, 1993.

[4] T. Vegge and T. Rasmussen, "Atomistic simulations of cross-slip of jogged screw dislocations in copper," *Philosophical Magazine Letters*, vol. 81, pp. 137–144, 2001.

[5] Y. Osetsky and D. Bacon, "Atomic-scale mechanisms of void hardening in bcc and fcc metals," *Philosophical Magazine*, vol. 90, no. 7-8, pp. 945–961, 2010.

[6] T. Hatano and H. Matsui, "Molecular dynamics investigation of dislocation pinning by a nanovoid in copper," *Physical Review B*, vol. 72, no. 9, pp. 1–8, 2005.

[7] T. Hatano, T. Kaneko, Y. Abe, and H. Matsui, "Void-induced cross slip of screw dislocations in fcc copper," *Physical Review B*, vol. 77, p. 064108, 2008.

[8] J. Langer, "Computing in physics: Are we taking it too seriously? or not seriously enough?" *Physics Today*, vol. 52, no. 7, pp. 11–13, 1999.

[9] F. Ercolessi, "A Molecular Dynamics Primer," *International School for Advanced Studies, Trieste, Italy*, 2001,
URL:http://www.sissa.it/furio/.

[10] Y. Osetsky, "An atomic-level model for studying the dynamics of edge dislocations in metals," *Modelling and Simulation in Materials*, vol. 427, pp. 268–280, 2003.

[11] M. S. Daw, S. M. Foiles, and M. I. Baskes, "The embedded-atom method: a review of theory and applications," *Materials Science Reports*, vol. 9, pp. 251–310, 1992.

[12] S. Plimpton, "Fast Parallel Algorithms for Short - Range Molecular Dynamics," *Journal of Computational Physics*, vol. 117, pp. 1–42, 1995.

[13] "LAMMPS: Large-scale Atomic/Molecular Massively Parallel Simulator,"
URL:http://lammps.sandia.gov.

[14] J. Li, "AtomEye: an efficient atomistic configuration viewer," *Modelling and Simulation in Materials Science and Engineering*, vol. 0393, no. 03, pp. 173–177, 2003.

[15] L. J. Hirth JP, *Theory of Dislocations*, 2nd ed. New York: McGraw-Hill, 1982.

[16] M. J. Whelan, P. B. Hirsch, R. W. Horne, and W. Bollmann, "Dislocations and Stacking Faults in Stainless Steel," *Proceedings of the Royal Society, Series A: Mathematical and Physical Engineering Sciences*, vol. 240, no. 1223, pp. 524–538, 1957.

[17] P. B. Heidenreich and W. Shockley, "Report of a Conference on the Strength of Solids," *London: Physical Society*, p. 57, 1948.

[18] M. S. Duesbery, "Dislocation motion, constriction and cross-slip in fcc metals," *Modelling and Simulation in Materials Science and Engineering*, vol. 6, no. 1, pp. 35–49, 1998.

[19] A. J. E. Foreman and M. J. Makin, "Dislocation movement through random arrays of obstacles," *Canadian Journal of Physics*, vol. 45, no. 2, pp. 511–517, 1967.

[20] U. F. Kocks, "Statistical treatment of penetrable obstacles," *Canadian Journal of Physics*, vol. 45, no. 2, pp. 737–755, 1967.

[21] R. Scattergood and D. Bacon, "The strengthening effect of voids," *Acta Metallurgica*, vol. 30, 1982.

[22] P. Hirsch and F. Humphreys, *The physics and strength of plasticity.* Cambridge, MA: MIT Press, 1969, ch. Plastic deformation of two-phase alloys containing small nondeformable particles, pp. 189–216.

[23] D. J. Bacon, U. F. Kocks, and R. O. Scattergood, "The effect of dislocation self-interaction on the orowan stress," *Philosophical Magazine*, vol. 28, no. 6, pp. 1241–1263, 1973.

[24] Y. Osetsky and D. Bacon, "Comparison of void strengthening in fcc and bcc metals: Large-scale atomic-level modelling," *Materials Science and Engineering: A*, vol. 400-401, pp. 374 – 377, 2005.

[25] M. S. Duesbery, N. P. Louat, and K. Sadananda, "The numerical simulation of continuum dislocations," *Philosophical Magazine A*, vol. 65, no. 2, pp. 311–325, 1992.

[26] M. Mendelev, M. Kramer, C. Becker, and M. Asta, "Analysis of semi-empirical interatomic potentials appropriate for simulation of crystalline and liquid al and cu," *Philosophical Magazine*, vol. 88, no. 12, pp. 1723–1750, 2008.

[27] Y. Mishin, M. Mehl, D. Papaconstantopoulos, a. Voter, and J. Kress, "Structural stability and lattice defects in copper: Ab initio, tight-binding, and embedded-atom calculations," *Physical Review B*, vol. 63, no. 22, pp. 1–16, 2001.

[28] C. Domain and G. Monnet, "Simulation of screw dislocation motion in iron by molecular dynamics simulations," *Phys. Rev. Lett.*, vol. 95, p. 215506, 2005.

[29] M. W. Finnis and J. E. Sinclair, "A simple empirical n-body potential for transition metals," *Philosophical Magazine A*, vol. 50, no. 1, pp. 45–55, 1984.

[30] G. J. Ackland, D. J. Bacon, A. F. Calder, and T. Harry, "Computer simulation of point defect properties in dilute fe-cu alloy using a many-body interatomic potential," *Philosophical Magazine A*, vol. 75, no. 3, pp. 713–732, 1997.